remote sensing

MDPI

Article

Landslide Mapping and Characterization through Infrared Thermography (IRT): Suggestions for a Methodological Approach from Some Case Studies

William Frodella *, Giovanni Gigli, Stefano Morelli, Luca Lombardi and Nicola Casagli

Department of Earth Sciences, University of Firenze, Via La Pira 4, 50121 Firenze, Italy; giovanni.gigli@unifi.it (G.G.); stefano.morelli@unifi.it (S.M.); luca.lombardi@unifi.it (L.L.); nicola.casagli@unifi.it (N.C.)

* Correspondence: william.frodella@unifi.it; Tel.: +39-055-275-7779; Fax: +39-055-205-5317

Received: 30 October 2017; Accepted: 5 December 2017; Published: 12 December 2017

Abstract: In this paper, the potential of Infrared Thermography (IRT) as a novel operational tool for landslide surveying, mapping and characterization was tested and demonstrated in different case studies, by analyzing various types of instability processes (rock slide/fall, roto-translational slide-flow). In particular, IRT was applied, both from terrestrial and airborne platforms, in an integrated methodology with other geomatcs methods, such as terrestrial laser scanning (TLS) and global positioning systems (GPS), for the detection and mapping of landslides' potentially hazardous structural and morphological features (structural discontinuities and open fractures, scarps, seepage and moisture zones, landslide drainage network and ponds). Depending on the study areas' hazard context, the collected remotely sensed data were validated through field inspections, with the purpose of studying and verifying the causes of mass movements. The challenge of this work is to go beyond the current state of the art of IRT in landslide studies, with the aim of improving and extending the investigative capacity of the analyzed technique, in the framework of a growing demand for effective Civil Protection procedures in landslide geo-hydrological disaster managing activities. The proposed methodology proved to be an effective tool for landslide analysis, especially in the field of emergency management, when it is often necessary to gather all the required information in dangerous environments as fast as possible, to be used for the planning of mitigation measures and the evaluation of hazardous scenarios. Advantages and limitations of the proposed method in the field of the explored applications were evaluated, as well as general operative recommendations and future perspectives.

Keywords: infrared thermography; landslide mapping; thermal anomaly; emergency management

1. Introduction

Landslide mapping, hazard assessment and risk evaluation are important goals for scientists, planners, decision makers and land developers [1].

In this context, the availability of new remote sensing technologies, based primarily on satellite, aerial and terrestrial remote sensing platforms, can allow systematic and easily updatable acquisitions of data over wide areas, and therefore may improve the production of landslide maps, reduce costs and optimize field work [2,3]. In recent years, amongst the new methods for accurate landslide mapping, ground-based technologies such as digital photogrammetry (DP) [4–6], terrestrial laser scanning (TLS) [7–9], ground-based interferometric synthetic aperture radar (GB-InSAR) [10–12] and infrared thermography (IRT) [13–15], have been increasingly used as efficient remote surveying techniques for the prompt characterization and mapping of slopes affected by instability processes. IRT (or thermal imaging) is the branch of remote sensing dealing with measuring the radiant temperature of the Earth's

surface features from a distance [16], and can map the pattern evolution of the investigated scenario's surface temperature. During the last decades, thanks to the technological development of portable high resolution and cost-effective thermal imaging cameras, this technique has undergone a significant increase of usage, in terms of sensor accuracy and spatial resolution, together with fast measurement, processing times and improved quality of the thermographic data. IRT offers non-contact, wide area detection of subsurface defects, and can be used as an alternative or complement to conventional inspection technologies in a wide variety of technical and scientific applications [17]. Since the 1980s, thermal infrared sensors have been used in environmental studies from terrestrial, airborne and spaceborne platforms, in the following contexts: mining [18], tunneling [19], detection of hydrological features in karst watersheds [20], monitoring of geothermal activity [21,22], mapping of geomorphic and sedimentary features of alluvial fans [23,24], agricultural soil analysis for evaluating the moisture content [25,26] and the land surface temperature patterns [27,28].

In volcanic monitoring, an exhaustive review on thermal imagery applied to volcanic monitoring is given by [16]. Furthermore, IRT has been widely used in industrial applications for the detection of defects in machines, cracks and fatigue of materials [29,30], as well as in the field of civil engineering and cultural heritage to detect delamination, subsurface cracks and the presence of water infiltration in concrete and masonry structures, also providing an effective tool to assess the integrity of historical buildings and masonry [31–37].

In the field of landslide surveying and mapping, detailed IRT studies are limited: the first pioneeristic investigations were conducted in the early 1990s [38,39], but then little further investigation took place until the early 2000s, when modern cost-effective and high resolution thermal cameras were developed. In this context [14] combined IRT with ground penetrating radar (GPR) surveys in order to detect eroded caves behind shotcrete-protected slopes overlooking a roadway, while many authors applied IRT from ground-based platforms (coupled with TLS, geophysical investigations and traditional field surveys) to the analysis of unstable slopes with the following purposes: (i) obtain information about the rock mass fracturing [40,41]; (ii) detect shallow surface weakness in rock walls [13]; (iii) map open fractures for rock slide and rock fall assessment [15,42–44]; (iv) map ephemeral drainage patterns [45–48]; and (v) perform geomechanical surveying of jointed rock slopes [49,50]. Applications of thermal imagery from airborne and satellite platforms in the field of landslide mapping are limited to multispectral and near-infrared [51,52]. In this paper, the use of IRT for the analysis of slopes affected by instability phenomena is presented. In particular, IRT was applied from both terrestrial and airborne platforms, in an integrated approach with TLS, GPS, accurate field surveys and optical imagery, in order to detect potential criticalities on unstable slopes, and therefore provide 2D and 3D slope-scale mapping and characterization. The final aim is to improve the investigative capacity of IRT and to extend its fields of application in landslide studies, in order to provide an effective and reliable tool for supporting the Civil Protection departments and the local authorities involved in landslide emergency management phases. In this context the potential of IRT was explored in various types of landslide scenarios and risk management contexts.

2. Theoretical Principles

IRT is based on the physical principle stating that any object having temperature higher than absolute zero produces electromagnetic radiation falling within the IR band (Figure 1). The latter is known as "thermal radiation", and can be remotely sensed and used to retrieve the radiant temperature of the analyzed scenario.

On the Earth surface almost all thermal radiation consists of IR in various wavelengths; therefore it is also termed "thermal infrared" energy [53]. IR radiation, which is primarily responsible for thermal radiation, falls within the wavelength range of approximately 0.74 μm to about 1000 μm, between the red end of the visible region and the microwave portion of the electromagnetic spectrum [17] (Figure 1a).

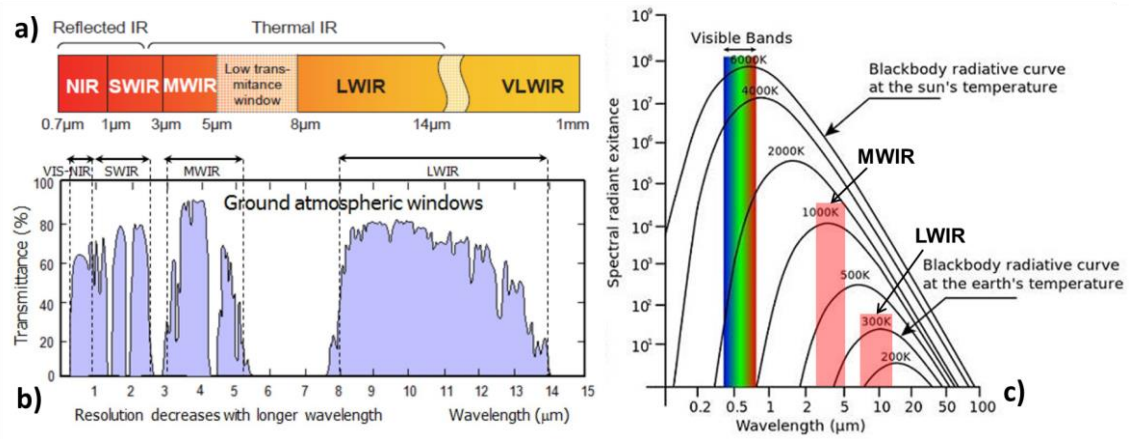

Figure 1. The infrared region of the electromagnetic spectrum (**a**) after [54]; (**b**) the spectral region between 0 and 15 μm, with the atmospheric windows and the infrared bands regions after [55]; (**c**) spectral distribution of energy radiated from blackbodies of various temperatures: red squares highlight the infrared bands used by the sensors of modern thermal cameras (Image credit: Ant Beck/CC-SA).

Even though there is not a widely accepted standard classification of the IR bands, their boundaries are chosen considering the wide applications of detectors sensible to IR radiation (Figure 1a). The main attenuation factors of thermal radiation commonly considered when dealing with thermal imaging are those related to atmospheric effects. In particular, infrared absorption by atmospheric molecules is significant in the 0–14 μm spectral region (Figure 1b), except for two spectral bands in which many thermal cameras are sensitive: (a) the spectral window between 8 and 14 μm, also called "Long-Wavelength Infrared band (LWIR)"; (b) the waveband between 3 and 5 μm, namely "Mid-Wavelength Infrared band (MWIR)", generally considered more suited to high temperature measurements [13] (Figure 1c).

IRT Theory

In accordance with the principle of the conservation of energy, the relationship between incident energy and its interaction with terrain elements, depending on wavelength, can be stated as:

$$Ei(\lambda) = E\alpha(\lambda) + E\rho(\lambda) + E\tau(\lambda) \quad (1)$$

where E_i = incident energy; E_α = absorbed energy; E_ρ = reflected energy; E_τ = transmitted energy, with all energy components being a function of wavelength λ. In order to describe the nature of thermal energy interactions the equation ratios can be defined as (i) Absorptance: $\alpha(\lambda) = E\alpha/Ei$; (ii) Reflectance: $\rho(\lambda) = E\rho/Ei$; Transmittance: $\tau(\lambda) = E\tau/Ei$.

Thus (1) can be restated in the form:

$$\alpha + \rho + \tau = 1 \quad (2)$$

This equation is an energy balance equation expressing the interrelationship among the mechanisms of absorption (α) reflection (ρ) and transmission (τ) of a terrain element. The radiative properties of a body, called emissivity, are denoted by the symbol ε [56,57]. The ideal source of thermal radiation is the "blackbody": a hypothetical, ideal radiator that totally absorbs all energy incident upon it and re-emits it, without reflection or transmission (ρ, τ = 0), as stated by the Kirchhoff Law on radiation:

$$\alpha(\lambda) = \varepsilon(\lambda) \quad (3)$$

Therefore, considering a blackbody the Formula (2) can take the form:

$$\varepsilon = 1 \quad (4)$$

This shows the corollary of Kirchhoff's Law on radiation: the emissivity cannot exceed one (because the absorptivity cannot, by conservation of energy), so it is not possible to thermally radiate more energy than a black body, at equilibrium. In most remote sensing applications, the objects we normally deal with are real bodies [58], also called "grey bodies" (objects that have constant emissivity for all wavelengths) [59], which are opaque to thermal radiation and emit only a fraction of the energy emitted from a blackbody at the equivalent temperature. Therefore, for grey bodies τ can be dropped from Equation (2) so that:

$$\varepsilon + \rho = 1;\ \rho = 1 - \varepsilon \quad (5)$$

This equation demonstrates the direct relationship between an object's emissivity and its reflectance in the thermal region of the electromagnetic spectrum. The lower the object's reflectance, the higher its emissivity and vice-versa. As infrared thermography operates within limited spectral ranges, in practice it is often possible to treat objects as grey bodies. The emissivity of a real material is a spectral quantity characterizing the nature of the surface of the object being imaged [13]. In detail it can be defined as a factor that describes its efficiency in radiating energy compared to a black body (radiant exitance of an object at a given temperature over the radiant exitance of a black body at the same temperature [56]).

This shows that ε can have values between 0 and 1. Many materials radiate like blackbodies over certain wavelength intervals: for example, water has $0.98 < \varepsilon < 0.99$ behaving very close to a blackbody radiator in the 6–14 μm wavelength range; soil and rocks are grey bodies with high emissivity values ($\varepsilon \geq 0.8$) [53]. At any temperature, a blackbody can emit the maximum energy possible per unit time in every part of the electromagnetic spectrum [13].

The concept of emissivity is of capital importance in the science of IRT, because it is the foundation for relating IR radiation to a real object's temperature, as stated by the Stefan-Bolzmann's Law:

$$W = \varepsilon \sigma T^4 \quad (6)$$

where W = total radiant exitance from the material surface, expressed in Watt/m^2; σ is the Stephan Boltzmann constant (5.6697×10^{-8} Wm^{-2} K^{-4}); T is the absolute temperature (expressed in K) of the emitting material. This law states that the electromagnetic energy emission (radiant power) per area unit of a body depends on the fourth power of the absolute temperature and on its value of emissity. This law is the basis for radiative heat loss estimates, and constitutes the theoretical basis for IRT [57].

3. Materials and Methods

Thermography is a type of infrared imaging accomplished with IR thermally calibrated cameras (Figure 2) capable of detecting radiation in the electromagnetic spectrum within the infrared wavelengths, and converting it in digital images of that radiation (thermograms or thermographic images) (Figure 3). It is important to state that the thermal sensors detect radiation from the surface (approximately the first 50 μ) of ground objects, which may not be indicative of their internal bulk temperature [53].

The main components of a thermal camera are: (i) lenses; (ii) sensor; (iii) built-in processor; (iv) camera firmware. The camera lenses (commonly made of Germanium and opaque to visible radiation) focus IR radiation onto the sensor (nowadays largely represented by focal plane array uncooled microbolometers, mainly because of cost considerations [58]), whose cells are heated and send an electronic signal to the processor; the latter through the camera firmware converts the signal into radiant temperature values through a calibration procedure, creating a thermogram.

Focal Plane Array (FPA) sensors are staring (not scanning) systems composed of a two-dimensional array of photo-sensitive pixels, whose response is a function of both the pixel position within the array

and the wavelength of the optical radiation [59,60]. Microbolometer sensors are made of a metal or semiconductor materials (amorphous silicon and Vanadium Pentoxide), and operate responding to radiant energy varying their temperature and electrical conductivity, according to the intensity of absorption of incident radiations [17].

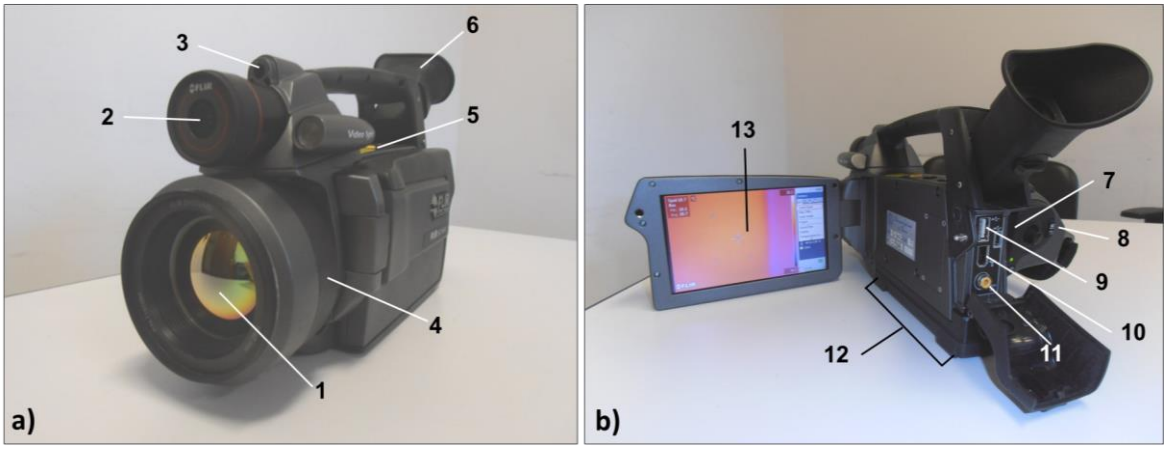

Figure 2. FLIR SC620 Thermal camera front view (**a**): 1 = germanium lens; 2 = digital camera; 3 = laser pointer; 4 = manual focus ring; 5 = control buttons; 6 = tiltable viewfinder. Back view (**b**) (7 = SD-card slot; 8 = built-in software buttons; 9 = USB connector; 10 = firewire connector; 11 = video connector; 12 = battery; 13 = LCD screen).

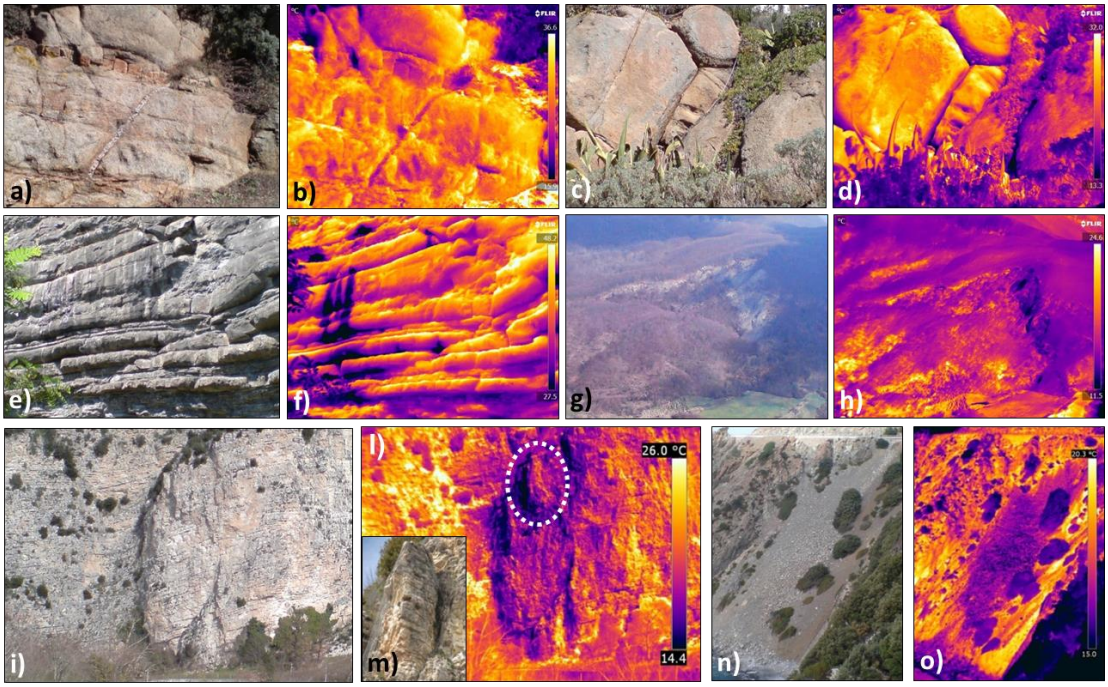

Figure 3. Examples of thermograms displaying thermal anomalies connected to slope instability phenomena in Italy. Dykelets and open fractures at Giglio Island, Tuscany (**a**–**d**); water seepage in sandstone layers (Fiesole, Tuscany) (**e**,**f**); aerial imaging of large landslide (San Benedetto Val di Sambro, Emilia Romagna) (**g**,**h**); unstable rock wall sector in (Val Nerina, Umbria) (**i**–**m**); debris apron along coastal cliff (Elba Island, Tuscany) (**n**,**o**).

Modern thermal cameras are designed and calibrated for a specific range of the IR spectrum: in thermal remote sensing applications, the prevalence of instruments operating at the 8–14 μm spectral

region (LWIR band) is due to the peak energy emissions for ambient Earth surface temperatures and to the presence of atmospheric windows (Figure 1c) [57]. The instrument employed within this work is a SC620 thermal camera (FLIR -"forward-looking Infrared"- systems, Wilsonville, OR, USA) [61,62] (Figure 2).

This device is characterized by an uncooled FPA microbolometer sensor, which can measure electromagnetic radiation in the thermal infrared band between 7.5 and 13 µm (see Table 1 for further technical specifications). A built-in 3.2 Mpixel digital camera allows for the comparison between IR and optical images, in order to improve the interpretation of thermal data. The product of an IRT survey is a pixel matrix, collected through the thermal camera array detector, which following the correction of the sensitive parameters (object emissivity, path length, air temperature and humidity) represents a surface temperature map of the investigated scenario. In Figure 3, pairs of images in the visible and thermal spectrum, displaying thermal anomalies connected to slope instabilities located in Italy, are reported. The surface temperature is represented by means of a color scale, namely "iron", in which the higher temperatures are displayed by the lighter colors, whereas the colder temperatures by the darker ones): leucogranitic dykelets (Figure 3a,b) and open fractures (Figure 3c,d) cross-cutting monzogranitic intrusions (Giglio Island, Tuscany, Italy); water seepage in sandstone layers (Fiesole, Tuscany, Italy) (Figure 3e,f); aerial imaging of large complex roto-traslative landslide (San Benedetto Val di Sambro, Emilia Romagna, Italy) (Figure 3g,h); unstable rock wall sector in thin layered limestones (Figure 3i,l), detail of protruding sector enhanced with dashed white oval (Val Nerina, Umbria, Italy) (Figure 3m); coarse debris apron along coastal cliff (Elba Island, Tuscany, Italy) (Figure 3n,o). The image processing procedures can be carried out before the image acquiring phase, through the thermal camera firmware, or in the post-acquiring phase by using specific thermographic software, i.e., [63]. The latter also allows for the following functions (Figure 4): (i) thermal focusing procedures (selecting the more appropriate temperature range of the thermogram in order to better visualize the scenario surface temperature pattern and possible anomalies); (ii) choice of the correct thermogram color scale (i.e., gray or iron-type color scales will highlight the temperature contrasts; algorithmic color scales can be more suitable to enhance temperature distribution and gradients); (iii) quantitative analysis on single pixels, scanlines, areas, or the entire thermogram matrix. Given the camera's spatial resolution and the scenario viewing distance, in order to picture a scenario wider than the camera's field of view (FOV) it is possible to mosaic adjacent thermograms with specific software (thermographic images must have at least a 50% of overlapping) [64].

There are two approaches regarding IRT analysis: (i) the passive approach; (ii) the active approach. The former tests materials and structures which are naturally heated by solar radiation, while with the latter an external stimulus is necessary to induce relevant thermal contrasts [17]. Within this work a passive approach was used. In the context of IRT applied for the analysis of slope instability phenomena, the presence within the observed surface of fractures, subsurface voids, moisture and seepage zones, will influence the material thermal characteristics (density, thermal capacity and conductivity) modifying its heat transfer [41]. Therefore, the presence of an inhomogeneity will be displayed in the corresponding radiant temperature map as an irregular thermal pattern with respect to the surroundings (a "thermal anomaly"). In slope instability phenomena, a qualitative analysis of thermographic images, based on the detection and interpretation of thermal anomalies can reveal the presence of potential criticalities such as (Figure 3): (i) structural discontinuities (due to the cooling/heating effect of air circulating within open fractures; different thermal transfer capacity of the infilling material with respect to the exposed sound rock); (ii) moisture or seepage zones (due to the surface cooling caused by water evaporation); (iii) ledge-niche protruding systems, scarps (due to the slope aspect and topographic roughness, which creates shadowing effects during a daily cycle of solar radiation); (iv) loose coarse debris cover sectors (due to the cooling effect of air circulating within the voids). Furthermore, multi-temporal thermographic surveys, characterized by a series of thermal images acquired at different solar illumination conditions (e.g., sunrise, midday, sunset, as well as intermediate times), can provide information about the thermal transfer efficiency of the analyzed slope

(heating-cooling phases) [14,40]. Since the thermal inertia of a sound rock is greater than that of a highly fractured rock or rock debris cover, the presence of discontinuities, voids or fracturing can be detected through a multi-temporal thermographic survey. Within this work, the potential of IRT for landslide mapping and characterization (used in a passive approach) was explored by analyzing different kinds of slope mass movements, such as rock slide-falls, earth flows and composite movements [64], located in the Italian territory (Figure 5, Table 2). The research activities were carried out from terrestrial and airborne platforms in combination with other geomatics methods (such as TLS and GPS), in order to establish an operative methodology to be used in various applications and risk management phases (Figure 6). In this context, the obtained products (2D-3D surface temperature maps) were analyzed for a qualitative detection of landslide criticalities (such as open fractures, seepage and moisture sectors), and geo-rectified to be used in a Geographic Information System (GIS). A quantitative analysis was also applied, by creating differential surface temperature maps in order to detect potentially unstable debris cones and ledge-niche systems, and by analyzing the 24 h average surface temperature evolution of different slope sectors. Depending on the hazard context of the study areas, the collected remotely sensed data were validated through field inspections. The adopted thermal calibration parameters (air temperature-humidity, distance and material emissivity) are reported in Table 2. Air temperature-humidity values were obtained by means of a pocket thermo-hygrometer. When the analyzed site was accessible (case studies 1, 2 and 3) experimental laboratory emissivity tests were performed on the rock samples, according to the FLIR systems recommendations [65] and the work of [66], showing a good accordance with bibliographic data [67,68]. Some of the research activities were performed in order to support local authorities in the framework of the post-hydrogeological disaster activities led by the Italian National Department of Civil Protection.

Table 1. FLIR SC620 thermal camera main technical specifications.

Feature	Unit	Value
Detector size	Pixel	640 × 480
Spectral range	µm	[7.5, 13]
Temperature range	C°	[−40, +500]
Thermal accuracy	C°	±2
Thermal sensitivity	mK	40
Field of view (FOV)	(°)	24 × 18
Lens	(°)	24
Spatial resolution	mrad	0.65
Minimum focus distance	m	0.3
Image frequency	Hz	30

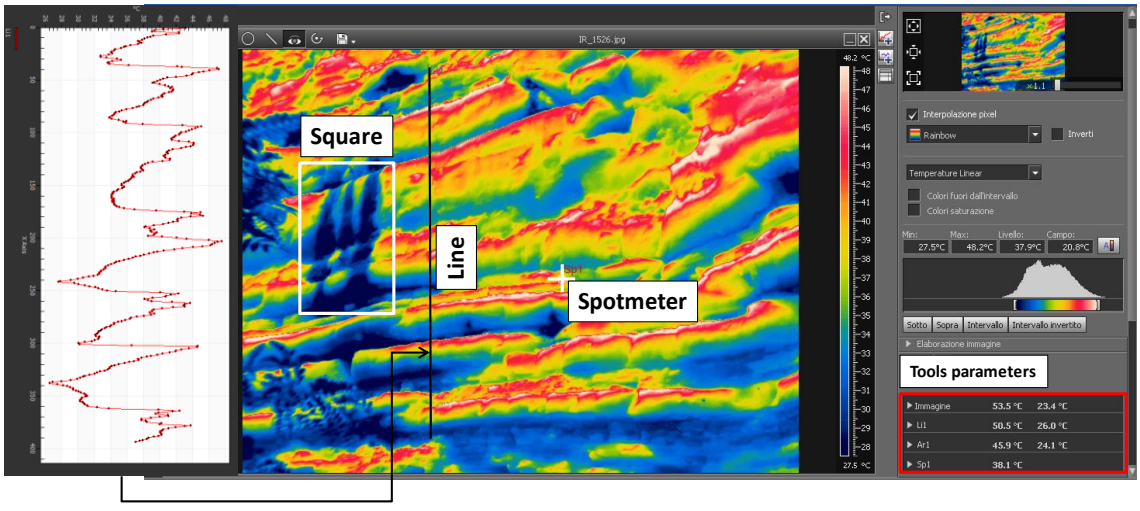

Figure 4. FLIR ResearchIR 3.4 sp3 software interface (FLIR, 2013).

Table 2. Study site and Infrared Thermography (IRT) survey characteristics.

Case Study N°	Study Site Region	Landslide Type	Lithology	Slope Aspect	Sensor-Target Mean Distance (m)	Image IFOV (cm)	Air Temperature (C°)/Relative Humidity (%)	ε	Survey Type
1	Piemonte	Rock slide	Dolostones-limestones	SE	500	33.3	25–33/40–53	0.94	Multi-temporal 8 h (heating phase)
2	Umbria	Rock slide	Micritic limestones	N	1000	66.6	17–41/20–54	0.95	Multi-temporal 48 h
3	Emilia Romagna	Rock fall	Organogenic calcirudites-calcarenites	N	300	19.5	21–36/39–58	0.95	Multi-temporal 48 h
4	Emilia Romagna	Roto-translational slide-flow	Muddy matrix with heterogeneous clasts	E-SE	300	19.5	24/52	0.92	IR image sequence (heating phase)
5	Sicily	Roto-translational slide/flow	Sandy-loamy matrix with heterogeneous clasts	SE	500	33.3	21/45	0.93	Multi-temporal (heating phase)

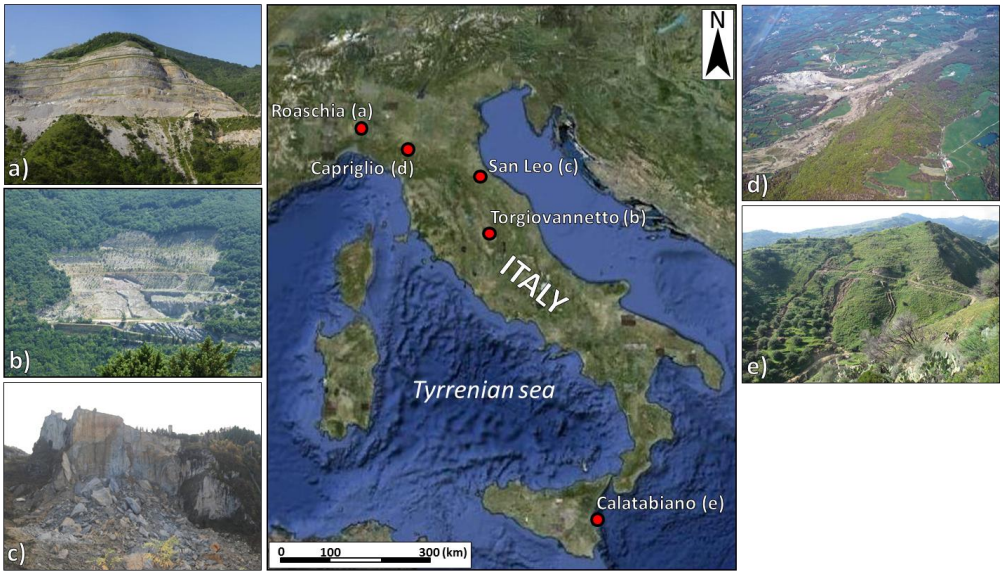

Figure 5. Location of the experimental sites: potential rock slide in active limestone quarry (**a**); active rock slide in an abandoned limestone quarry (**b**); rock fall-affected sub-vertical organogenic-calcarenitic cliff in cultural heritage site (**c**); large fast moving earth flow threatening villages and roadways (**d**); a composite earth slump-flow which damaged a water pipe transect of the Messina city acqueduct (**e**).

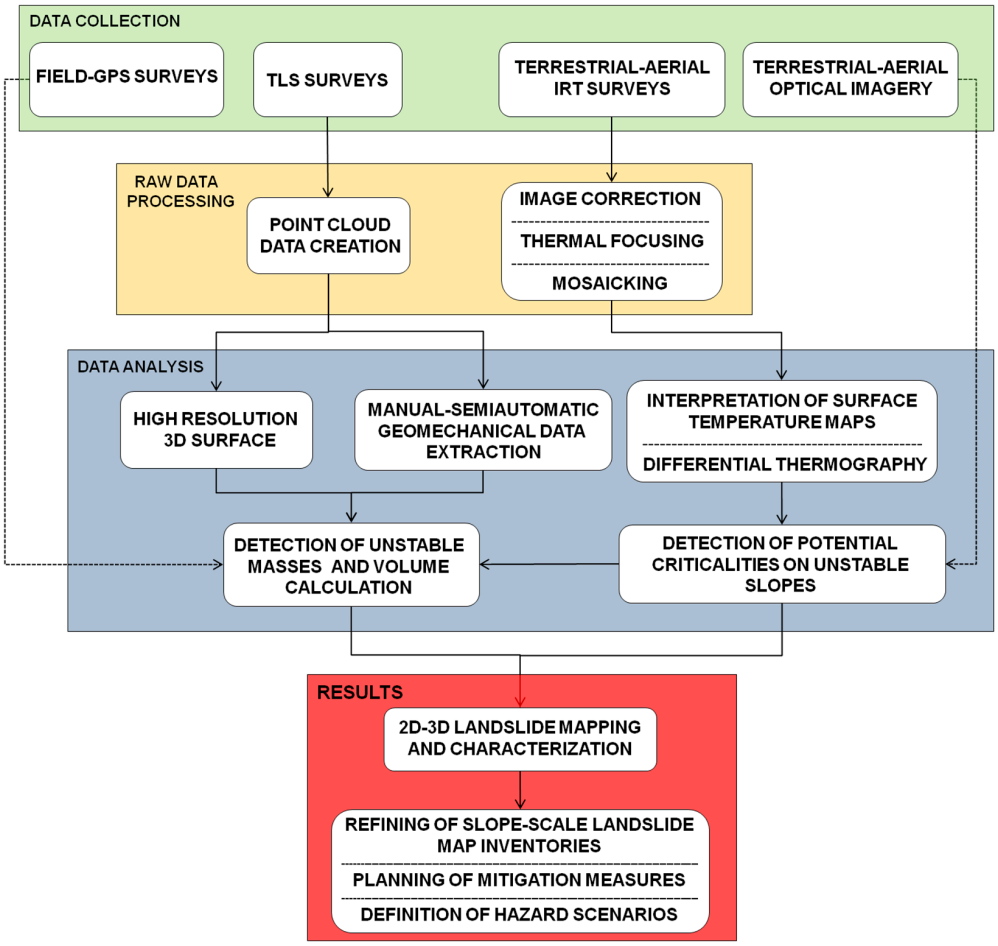

Figure 6. Workflow of the implemented methodology.

4. Results

4.1. Mapping Potentially Unstable Rock Wedges (Case Study 1)

The first case study is a mainly dolomitic-limestone active quarry (Figure 5a; Table 2) where field inspections had highlighted a low angle dipping mesoscopic fault system, isolating a potentially unstable rock wedge. A short-term multi-temporal IRT survey and a TLS acquisition were carried out at a 500-m distance from the investigated quarry sector. Thermograms were acquired from 8 a.m. to 1 p.m. in the month of July 2011 in order to analyze the slope gradual heating due to solar radiation (heating phase). The obtained surface temperature maps revealed cold thermal anomalies in correspondence to the lowermost slope sector (Figure 7a,b), not detectable in the corresponding optical image (Figure 6c), whose pattern is congruent with the investigated fault system. With the aim of analyzing the slope surface thermal variations, a differential surface temperature map was generated in a MATLAB environment by subtracting the above-mentioned thermograms pixel-by-pixel (Figure 7d). This product allowed enhancing loose coarse-grained debris cones in the lowermost slope sector, which are characterized by higher thermal transfer capacities with respect to sound rock, due to the presence of air circulating within the voids (Figure 7d). Furthermore, the fracture pattern was traced on the high resolution geo-referenced TLS 3D surface, providing an accurate 3D fracture map (Figure 8a). The 3D fracture net allowed an accurate reconstruction of the most critical sliding surface. Finally, through a quantitative comparison between the latter and the high resolution surface, a thickness map of the investigated rock wedge was created in a Riscan Pro software environment [69] (Figure 8b), leading to an estimate of 340,000 m^3 of the potentially unstable volumes involved.

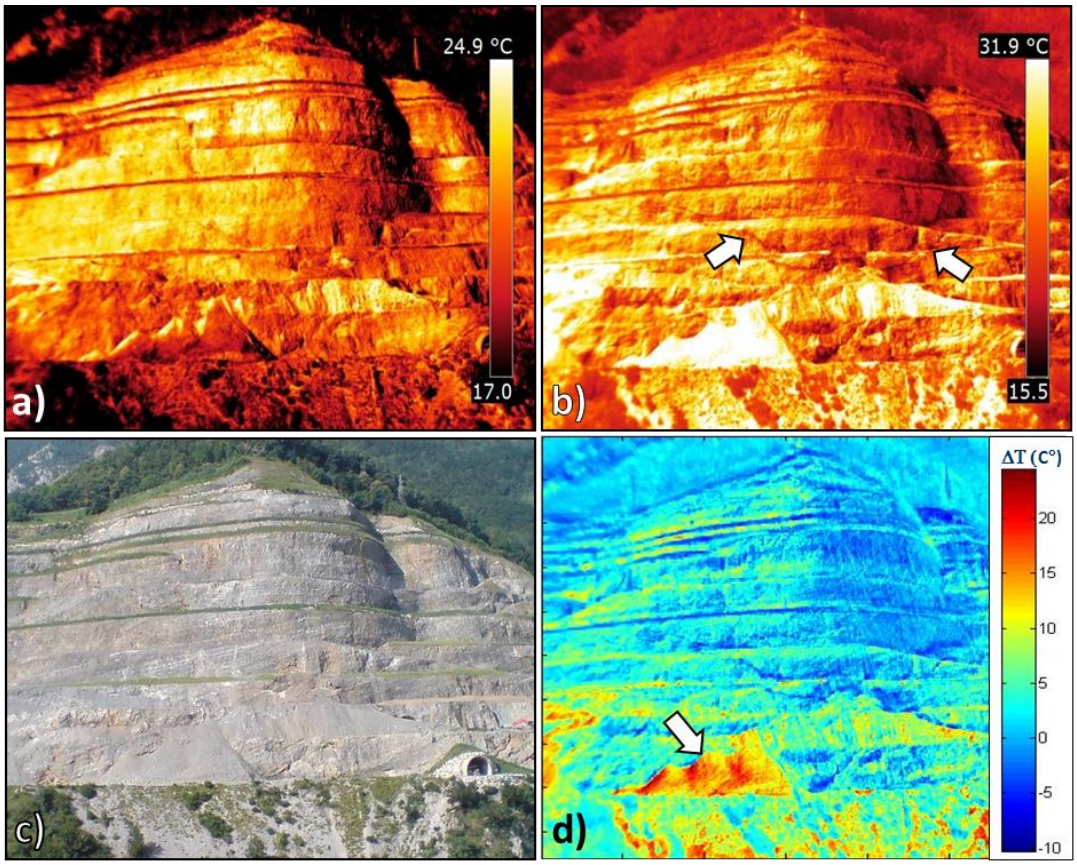

Figure 7. 2D surface temperature maps of the investigated quarry sector acquired at h 08:00 (**a**) and 13:00 (**b**) in the month of July. Optical image acquired by the built-in digital camera (**c**) and 2D differential surface temperature map (**d**) between (**a**,**b**).

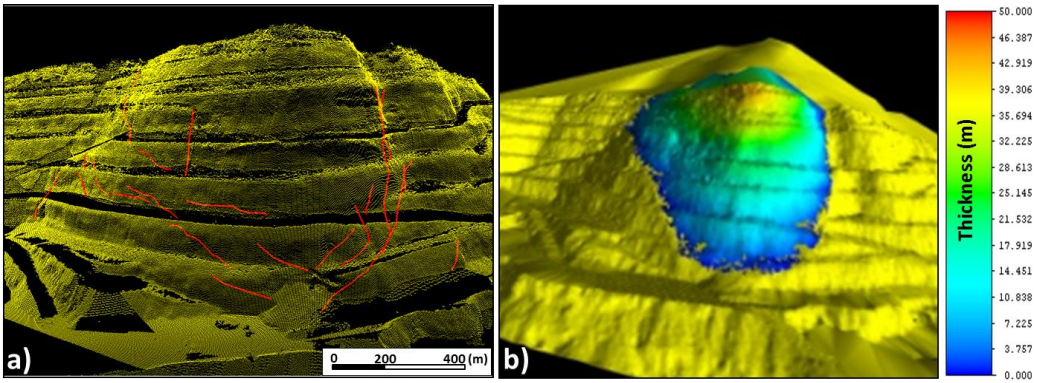

Figure 8. 3D maps of the investigated quarry sector: (**a**) fracture pattern traced on terrestrial laser scanning (TLS) point cloud; (**b**) thickness of the potentially unstable wedge on high resolution surface.

4.2. Multi-Temporal IRT Survey for Complex Fracture Pattern Mapping in Active Rock Slide (Case Study 2)

The Torgiovannetto abandoned quarry (Figure 5d, Table 2) is characterized by well stratified thin micritic limestone layers, alternating with clayey interbeds, centimetric in thickness. The quarry front, having an elevation drop of about 140 m, is affected by a rockslide (182,000 m^3 in volume), too large to be stabilized (Figure 9) [70,71]. The unstable rock wedge (roughly trapezoidal in shape) is delimited by three persistent fractures (Figure 9b,c): (i) a sub-vertical back fracture with an E-W strike, which in some sectors displays a width up to 2 m (F1); (ii) a downhill boundary, corresponding to a clayey interbed (355°/24°), cutting the quarry front obliquely and acting as basal sliding surface (F2); (iii) the western side of the landslide is non-continuously delimited by a system of open fractures (F3), mainly belonging to a sub-vertical discontinuity set (82°/74°). This latter fracture system has a complex pattern and is not fully developed thus leaving rock bridges (Figure 9d,f).

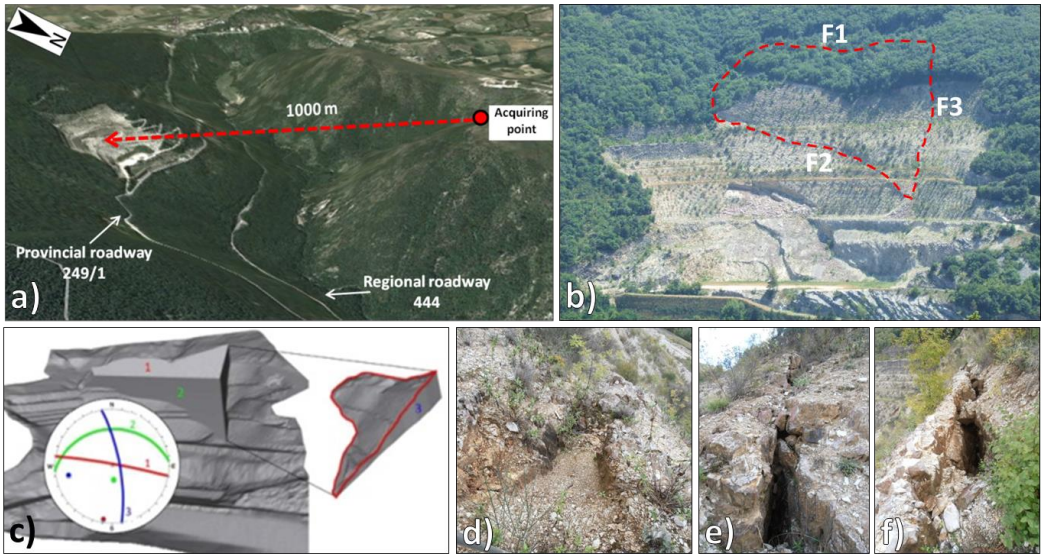

Figure 9. Thermographic survey installation point (**a**); view of the quarry front: in red a rough delimitation of the unstable wedge (**b**); TLS 3D representation of the sliding block and stereographic projection of the main planes delimiting it (**c**), after [68]; pictures of the lateral fracture pattern (F3) from bottom (**d**) to topmost sectors (**e**,**f**).

With the aim of defining the unstable rock wedge deformation field and precisely assessing its boundaries, a multi-temporal IRT survey (24-h cycle) was carried out. The selected installation point

(set at an average 1000 m distance) gave a coverage of the whole quarry front, providing the pattern detection of two of the wedge fractures (F2 and F3; Figure 9a,b). The rock wedge back fracture (F1) was not visible in the thermograms due to the dense vegetation cover. Selected thermograms enhanced cold thermal anomalies in correspondence with both the surveyed landslide boundaries (Figure 10a,b). In order to accurately locate the detected fractures on the slope surface, a 3D surface temperature map was created by merging the thermographic data with a previously acquired TLS geo-referenced 3D surface (Figure 10c) [44,71]. For this purpose, the thermographic images were manually registered in a Riscan Pro environment by defining the relations between 3D object points and the homologous points on the thermogram. Once the transformation matrix was calculated for each thermogram, the high resolution mesh was textured, making it possible to draw the true 3D shape of the analyzed elements, which are therefore geo-rectified and can be used in GIS systems for accurate mapping.

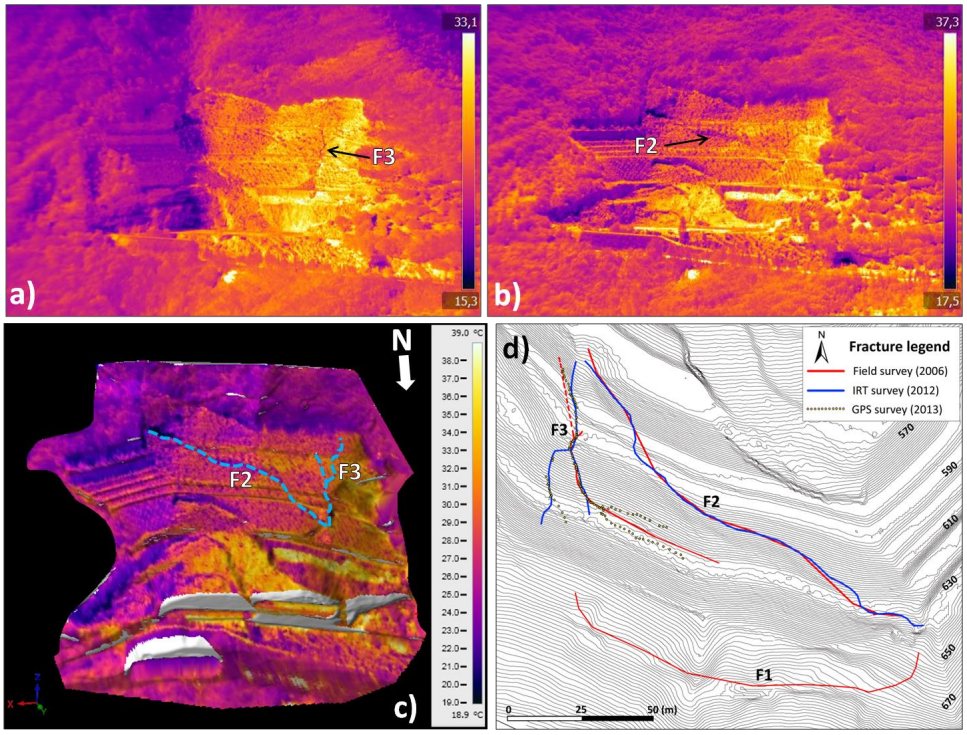

Figure 10. Quarry front thermographic images acquired on July 2012 ((**a**); early morning; (**b**); noon); 3D surface temperature map acquired at h 13.00 in the month of July 2012 (**c**) (F1 = downhill boundary; F2 = western boundary; F3 = lateral fracture); (**d**) Fracture map of the rock wedge.

To give an example of the advantages deriving from the analysis of the 3D surface temperature map, the obtained 3D fracture pattern was projected on the quarry front topographic map, and compared with the fracture system mapped through a field survey, carried out in 2006 [71], and a GPS survey, carried out in 2013 (Figure 10d). This comparison demonstrated that the remotely sensed data showed a good accordance with the data coming from the field surveys: in particular, the mapping accuracy of fracture F3 was improved, showing a more continuous pattern (probably connected to the evolution of the deformation field since 2006, due to the rupture of rock bridges in that sector of the rock wedge).

4.3. Multitemporal IRT Survey for Seepage and Ledge-Niche Systems Detection (Case Study 3)

The historical town of San Leo (Figure 5c; Table 2) is located on top of an isolated rock massif made of limestone-arenaceous formations, bordered by sub-vertical cliffs up to 100 m high, which overlies soft ductile clayey deposits [72]. For its geomorphological and geological setting the site is historically

affected by instability phenomena: rock falls, slides and topples had taken place in correspondence of the massif boundaries, with consequent retreat of the bordering cliffs and their continuative shaping due to the formation of ledges, overhangs and niches [73]. This process was furthermore worsened by piping erosion due to water percolation along the rock mass discontinuities and to the consequent development of springs at the foot of the cliffs, along the contact with the underlying impermeable clayey bedrock [74]. On 27 February 2014 an entire portion of the rock plate's north-eastern sector collapsed causing a huge rock fall. In correspondence to the massif collapse-affected sector, this rock fall event caused a consistent retreat of the cliff edge, putting some buildings located in the town northern sector at high risk. Minor rock fall events kept taking place on the newly formed rock wall, worsening this hazardous situation. Following this event, a GB-InSAR monitoring activity coupled with TLS surveys was carried out in order to manage the post-event emergency phase and evaluate the residual risk [72]. In this context, IRT surveys were also carried out to integrate the TLS rock mass characterization, with special regards to the rapid assessment of the hydraulic conditions along critical discontinuities, in order to obtain a qualitative estimate of the seepage parameter [75]. Surface temperature maps collected on 9 April 2014 (following a period characterized by intense local rainfall) showed widespread seepage sectors in correspondence to a key rock mass discontinuity, corresponding to a high persistent normal fault dissecting the whole rock massif (oval 1 in Figure 11a). Minor seepage sectors (ovals 2, 3, 4 in Figure 11a) were also detected in correspondence to rock wall sectors affected by a widespread fracture network [72], and the occurrence of minor rock falls (Figure 11d).

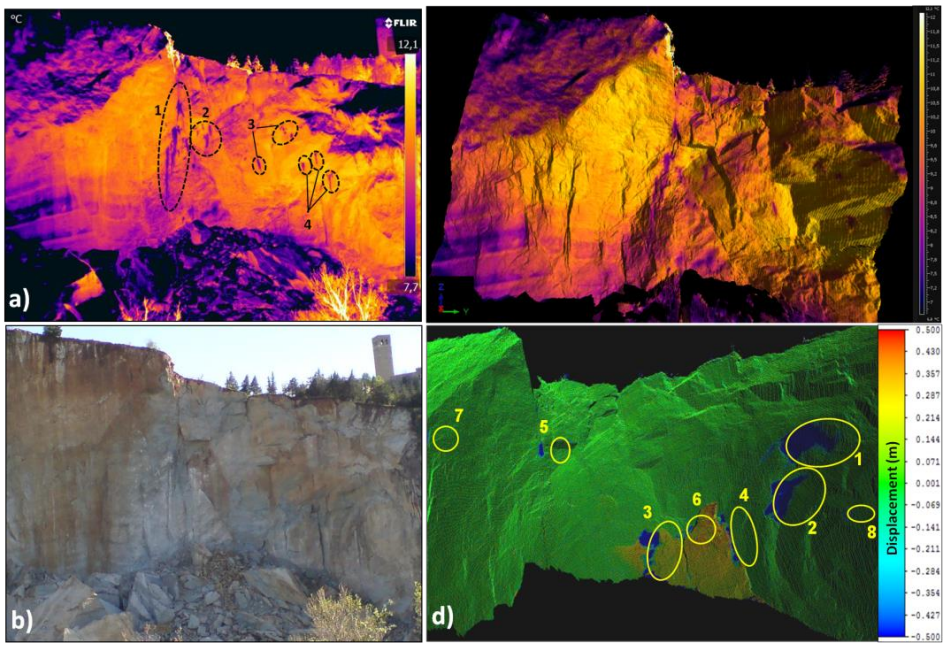

Figure 11. Thermogram of the San Leo rock cliff acquired on 9 April 2014 (**a**), with corresponding optical image (**b**). Obtained 3D surface temperature map (**c**) (seepage sectors 1–4 are highlighted by black dashed ovals). Comparison between 7 March 2014 and 18 December TLS scans (**d**), locating the occurring detached rock block sectors (in yellow) and rock wall sector characterized by toppling phenomena (orange-yellow areas), after [3,72].

Furthermore, a multi-temporal 24 h cycle IRT survey was performed in a dry period (11–12 June 2014; Figure 12), in order to analyze the surface temperature evolution of the rock cliff. The average values of surface temperature were calculated in correspondence to different rock cliff sectors (sound rock, fractured sectors, rock fall deposits) within all of the thermographic dataset (Figure 11c). The obtained graph shows how the daytime surface temperature curves of the four sectors are heavily influenced by the slope's aspect, which does not allow for a continuous surface heating, while the cooling phase of

the rock wall is more regular during the night. Nonetheless it is possible to observe how, during the heating phase, surface temperature variations of fractured rock or rock fall deposits are higher with respect to sound rock, due to its higher thermal inertia [23,40].

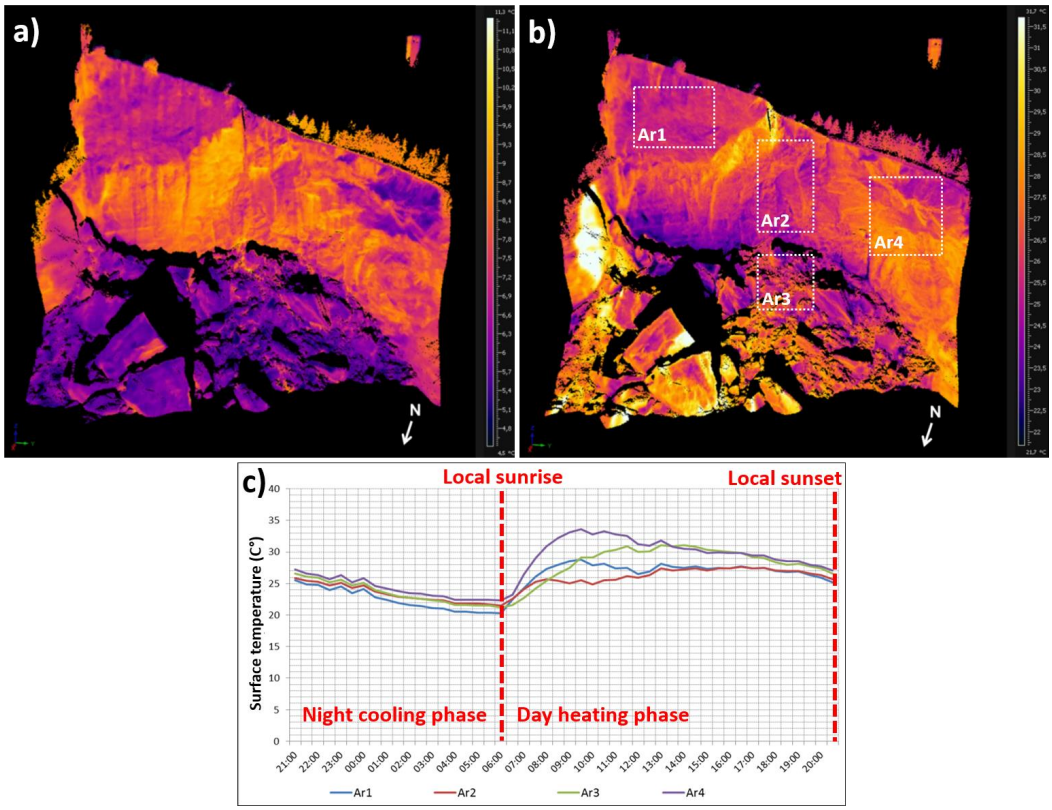

Figure 12. 3D surface temperature maps of the San Leo rock cliff: 11 June 2014, h 20:30 (**a**), 12 June 2014, h 05:00 (**b**), graph showing the 24 h average surface temperature evolution of different rock cliff sectors (Ar1: sound rock; Ar2; Ar4: intensively fractured sectors; Ar3 rock fall deposits) (**c**).

Finally, a 3D differential surface temperature map of the rock mass cooling phase was obtained (Figure 13a), directly showing surface rock mass sectors characterized by different ΔT values on the TLS 3D. Again, sound rock sectors are generally highlighted by low surface temperature variations (light blue areas in Figure 13a), while the highest surface temperature variations are located in correspondence to: open fractures, niches and overhangs, representing potential critical sectors regarding rock fall phenomena (red areas in Figure 13a).

These criticalities are associated to discontinuity sets (Bedding = BG; subvertical fracture = JN2, JN3) (Figure 13b,c), where minor block detachments had occurred (Figure 11d).

4.4. Aerial IRT Surveys for Landslide Ponds-Drainage Network Mapping (Case Study 4)

The Capriglio landslide is a large earth flow located in the Northern Apennines (Figure 5d, Table 2), which was triggered in April 2013 by prolonged rainfall and snowmelt [76,77]. The landslide is constituted by two main adjacent enlarging bodies with a roto-translational kinematics; they activated in sequence and subsequently joined into a large earth flow, channelizing downstream of the Bardea Creek for a total length of about 3600 m (Figure 14a–c). In the crown area, the landslide completely destroyed a 450-m sector of provincial roadway S.P. 101, and its retrogression tendency endangered the villages of Capriglio and Pianestolla, located in the upper watershed area of the Bardea Creek (Figure 14b). In addition, the landslide toe evolution was threatening the Antria bridge of the "Massese" 665R provincial road, over the Bardea Creek (Figure 13c). In the context of the surveying activity

carried out during the emergency management, on 5 May 2013, aerial thermographic and photographic surveys were conducted to perform a preliminary landslide boundary assessment.

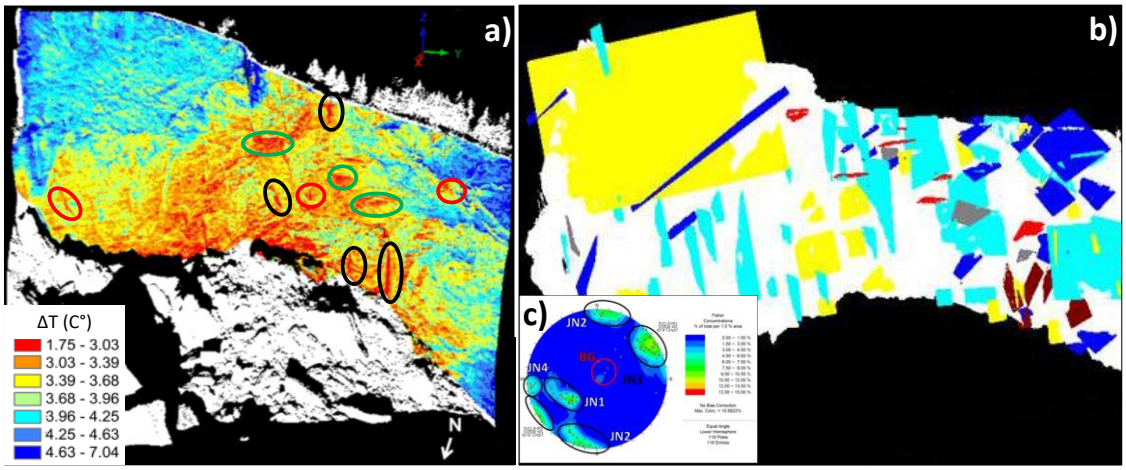

Figure 13. 3D differential surface temperature map highlighting open fractures (black ovals), niches (red ovals) and overhangs (green ovals) (**a**); manual extraction of discontinuity set on high resolution 3D surface (**b**) and resulting stereographic projection (**c**).

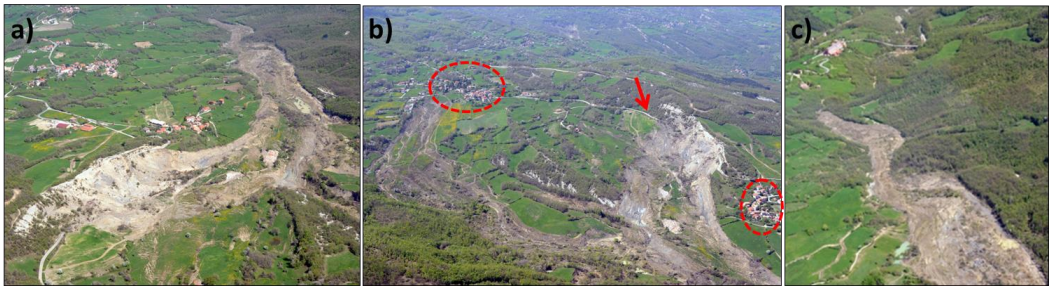

Figure 14. Aerial picture of the Capriglio earthflow (**a**); landslide upper sector (**b**) showing the villages of Capriglio (dashed oval on the left) and Pianestolla (dashed oval on right), were a transect of the local roadway was destroyed (highlighted by the red arrow); the landslide toe (**c**).

Field and GPS surveys were also conducted to integrate the aerial survey. An IR high frequency image sequence (30 frames/s) was acquired from a mean height of 300 m (leading to a 20 cm spatial resolution). Thermograms were sequentially extracted from the sequence to be focused, analyzed and mosaicked (Figure 15b). A sequence of high resolution digital images picturing the same scenario was used to improve the interpretation of thermal data (Figure 15a). To avoid geometric distortions, the IRT airborne survey was carried out by mounting the thermal camera over the aircraft hatch, so that the camera line of sight would be in as perpendicular a direction as possible with respect to the topographic surface. The line of flight was aligned along the landslide longitudinal axis at an average altitude of 300 m above ground level, leading to an image geometric resolution of about 20 cm. A manual mosaicking and geo-referencing procedure was performed in a GIS environment, by using omologous points between the overlapping thermograms and using a previously acquired Digital Elevation Model (DEM)and aerial optical image of the Emilia Region as a base reference map. The surface temperature map highlighted cold thermal anomalies in correspondence to the landslide drainage pattern and ponds, also showing a clearly visible temperature gradient from the dry upper sector (detachment area) to the colder wet toe (Figure 15a,b). The mapped thermal anomalies were compared and integrated with the high resolution mosaicked optical image: the resulting drainage-pond map, shown in Figure 15c.

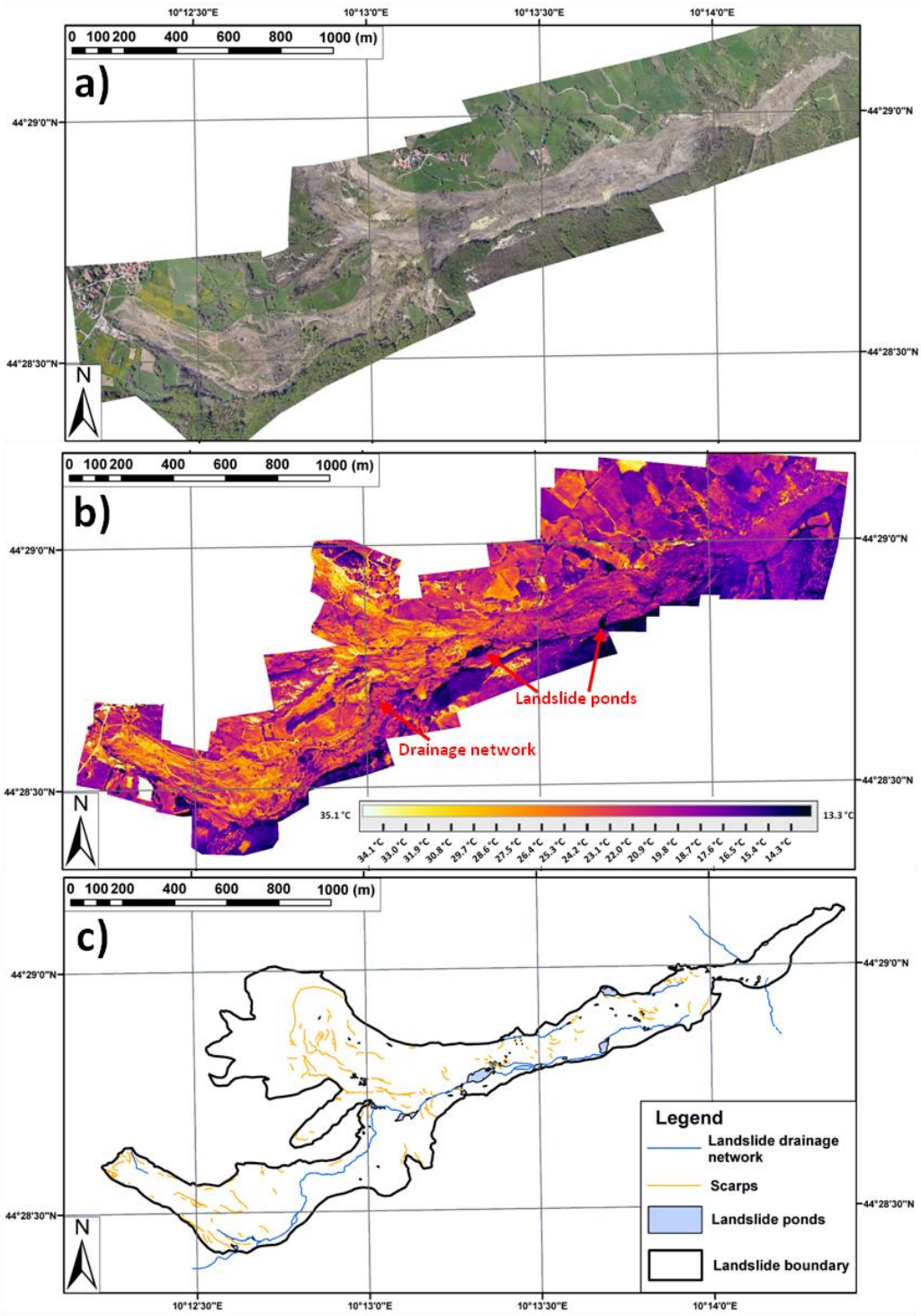

Figure 15. Mosaicked high resolution aerial optical image (**a**), acquired through a Nikon D-600 camera, and surface temperature map (**b**) of the investigated earth flow; (**c**) resulting map of the landslide ponds, drainage network and scarps.

4.5. Remote Landslide 3D Mapping for Emergency Management (Case Study 5)

This case study presents an example of the advantages given by IRT, used in an integrated approach with TLS and GB-InSAR, in order to manage a landslide post-emergency phase. The latter phenomena, occurring on 24 October 2015, causing the rupture of a water pipeline of the Messina city aqueduct system (Figure 5e, Table 2, Figure 16a). This event caused a considerable lack in water

supplies for many of the city inhabitants. In this context, an integrated monitoring network was implemented in order to assess the residual risk by analyzing the landslide's geomorphological and kinematic features, and to support the early warning procedures needed to ensure the safety of the personnel involved both in the realization of the aqueduct by-pass and the long-term landslide stabilization works [78,79]. The landslide, characterized by a roto-translational movement, involved a few meters in thickness of detrital slope deposits and developed for about 110 m in length and 65 m in width (Figure 16a). Minor scarps developed in the middle-lower landslide sector, while two erosional channels, formed by mud flows which almost reached the creek valley, delimited the landslide right and left flanks. The creek valley is located just a few hundred meters from the northern sector of the Calatabiano inhabited area, determining a high risk for the local population in case of eventual landslide reactivations. In order to integrate GB-InSAR and TLS surveys for mapping and characterizing geomorphological features of the Calatabiano landslide, daily IRT surveys were also carried out from the monitoring system location, from 10 to 12 November 2015. Since the thermal camera sensor field of view was not able to cover the entire landslide scenario, three single thermograms were analyzed and mosaicked, and rectified on the slope 3D surface, creating a high-resolution landslide 3D surface temperature map (Figure 16b). This advanced product enhanced low temperature values in correspondence to the right and left landslide flanks, due to the presence of moisture connected to the erosional channels thalweg. The landslide crown pattern and slope breaks were also highlighted by the obtained map. Cold areas were also detected in correspondence to the slope's vegetated and shadowed areas, while the higher surface temperature values were measured in correspondence to bare soils sectors and rocky outcrops. All of the collected remote sensing data were integrated, generating an accurate 3D geomorphological landslide map (Figure 16c), with the aim of accurately locating the recorded displacements with respect to the landslide geomorphological features and to the excavation activities, and detect the more critical sectors of the monitored slope.

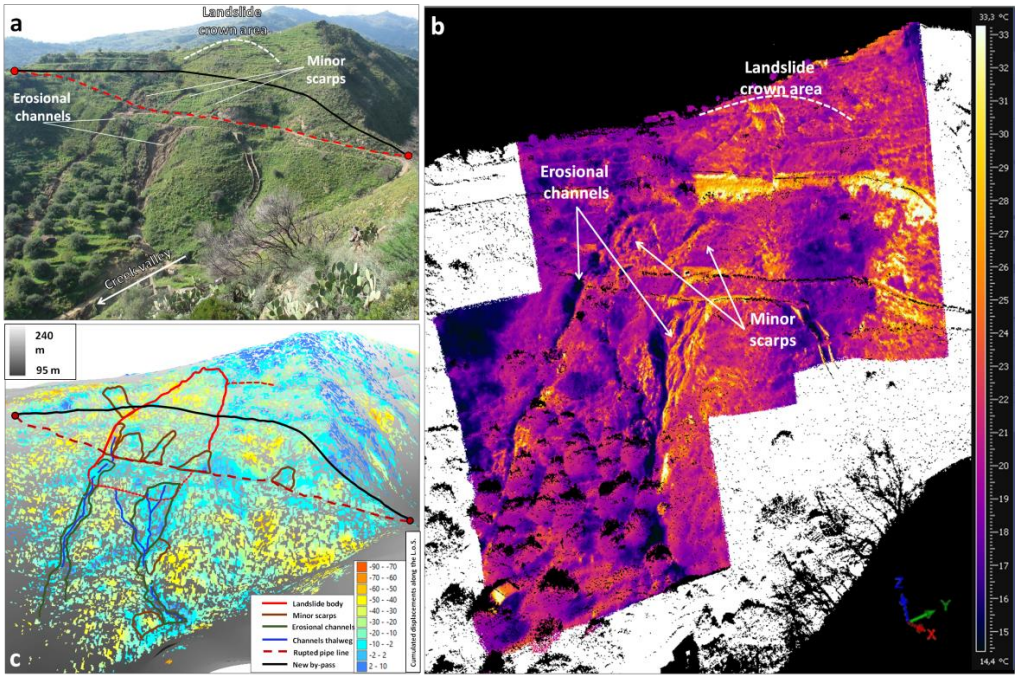

Figure 16. Image of the Calatabiano landslide acquired on 10 November 2015 from the monitoring system installation point (**a**) (the dashed white line represents the main landslide crown, the dashed red line represents the rupted pipeline); 3-D surface temperature map of the landslide area projected on TLS point cloud acquired on 12 November, h 13:00 (**b**); The Calatabiano landslide 3D geomorphological map, projected both on high resolution DEM, obtained by means of the TLS survey, and on GB-InSAR cumulated displacement map (**c**); after [78,79].

5. Discussion

Landslide maps can document the extent of landslide phenomena from a small or large watershed to a regional scale, and show information that can be exploited to determine landslide susceptibility, hazard, vulnerability and risk, as well as study the evolution of landscapes dominated by mass-wasting processes [2,80,81]. Mapping landslides using the traditional geomorphological field approach is part of the standard knowledge process on which all the application products are based [82]. Nevertheless, this procedure is hampered by the difficulty of detecting features of instability phenomena in the field due to: (i) the size of the landslide (often too large to be accurately surveyed); (ii) the viewpoint of the researcher (often unsuitable to observe all of the landslide sectors with the same level of detail); (iii) the strong influence of external causes (thick vegetation cover, dismantling and erosional processes and anthropic activities) [83]. For these reasons, a distant remote surveying point of view on unstable and hazardous areas can provide both the safety of the operator and a more accurate and complete landslide mapping [2]. The landslide mapping process is typically carried out through field inspections, which can be particularly problematical in hazardous areas with limited access. The Civil protection authorities, who are appointed to prevent landslide hazards and to manage emergencies deriving from potentially damaging events, need monitoring strategies that include reliable techniques for acquiring and processing data in a short period of time during the prevention and emergency management phases.

5.1. IRT Applied to Unstable Slopes Mapping and Characterization

The characteristics of rock slope failures are determined by the role of the rock structure, the dominant mechanism and kinematics, and the mechanical properties of the rock mass [84]. Fractures in particular are crucial factors for rock slope stability: open cracks can indicate initial stages of motion for deep-seated rockslides [85], while loosened rock sectors and ledge-niche systems represent potential instability zones along rock cliffs, as they are key indicators of future potential rock fall phenomena [13]. Furthermore, the effect of water seeping along rock masses can result in lowering the stability of rock slopes, by generating water pressure and weathering along discontinuities, reducing the shear strengths of rock mass fractures [75].

In this context, it is very important to rapidly and accurately assess the volume of an incipient rockslide, as this is one of the main factors controlling the runout in the case of catastrophic failure [86,87]. In the analysis of loose landslide deposits, experimental studies on thermal information derived from sensors working in the 8–12 μm spectral range, proved that considering the same land cover type the surface temperature measured is slightly lower with respect to stable areas [2]. Mapping of deformational and hydrologic features on earth flows can provide the identification of kinematic elements within the earth flow, and the geometry of the basal-slip surface [88]. Accurate remote mapping can provide important information for the involved local authorities and technicians (area and volume of unstable masses) for the preparation of landslide susceptibility and hazard models, with special regards to the planning of mitigation works. Moreover, the identification of unstable areas in landside-affected slopes can enable preventive countermeasures to be deployed, saving property and lives in more vulnerable areas. In the presented case studies, the proposed methodology provided the 3D mapping of complex fracture systems, leading to the evaluation of the potential unstable rock wedges volumes (case studies 1–2). In case study 3, IRT proved its effectiveness together with the TLS semiautomatic analysis in contributing to a more detailed remote 3D geometrical and geomechanical characterization, while the obtained 3D surface differential map provided a useful product to highlight potential unstable sectors. In case study 4, the mosaicked aerial thermograms led to the detection of thermal anomalies which were compared and integrated with the high resolution mosaicked optical images. This led to the mapping of earth flow ponds, drainage network and scarps. The aerial surveys were also fundamental both for the estimation of the landslide areas, and to monitor the flow evolution, showing that besides the located elements at risk (villages of Capriglio and Pianestolla), the fast evolution of the landslide toe was threatening a bridge of a provincial roadway. Finally, in case

study 5, the 3D landslide geomorphological map contributed to the understanding of the kinematic mechanisms involving the landslide mass, and to assess the landslide areal distribution and its volume. The proposed methodology proved to be an effective tool for landslide 2D and 3D surveying, mapping and characterization, especially in the field of emergency management, when it is often necessary to gather all the required information in dangerous environments as fast as possible, to be used for the planning of mitigation measures and the evaluation of hazardous scenarios.

5.2. IRT Surveying Technical and Logistical Contraints

In an IRT survey, the acquired radiant temperature does not correspond exactly to that emitted from the targeted object, due to the sensor-target distance and the related attenuation and scattering by air molecules, together with the sensor's thermal resolution, solar reflections and calibration errors [53]. In order to perform the correction of raw thermographic data, which display the so called "apparent radiant temperature", and obtain a "real radiant temperature" image, it is fundamental to choose the correct object emissivity values and remove atmospheric attenuation effects.

The best results are obtained when a thermographic operator is diligent in entering known values for all the pertinent variables: (i) emissivity of the object; (ii) air temperature and humidity; (iii) distance between the sensor and the target [65]. While the last variables are easily obtainable in the field (by means of a thermo hygrometer and a distometer) emissivity can vary according to several factors: (i) the material surface roughness (the greater the roughness compared to the size of the incident wavelength, the greater the absorption and emission); (ii) the moisture content (the more moisture contained within an object, the greater its ability to absorb and emit); (iii) the viewing angle from which the object is surveyed [89–93]. In most applications, the emissivity of an object is based on values found in tables and literature (in many cases also the camera firmware has its own emissivity table) [67,68]. However, when reasonably precise material emissivity values are needed it is possible to use an empirically developed approach to obtain them [65,66]. In case an accurate emissivity value cannot be obtained for grey bodies a standard value of 0.95 is recommended [65]. In a thermogram matrix, the smallest detectable object (IFOV = instantaneous field of view), corresponding to the image geometrical resolution, is determined by the distance between the sensor and the target (i.e., the thermal camera used in this work has 0.65 mrad spatial resolution, meaning that at a distance of 1 m from the object the IFOV is 0.65 mm). Therefore, in the planning of an IRT survey, given the possible logistical limitations (i.e., if the observation points are located in inaccessible areas), the position of the thermal camera acquiring point must be carefully considered in order to obtain both the best thermogram geometrical resolution and the field of view of the investigated scenario (Table 2).

5.3. IRT Benefits and Disadvantages

In accordance with the studies conducted by [14,31], in the field of landslide analysis IRT displays the following benefits and disadvantages:

1. Remote sensing: no direct contact is required between the camera and the investigated scenario, therefore permitting the measurement of hazardous areas safely.
2. Visibility: no external source of illumination is necessary, both diurnal and nocturnal operations are possible. Thermal radiation can also penetrate smoke and mist better than visible radiation.
3. Large monitoring capacity: IRT is capable of simultaneously measuring temperature in correspondence to different points within a scenario.
4. Portability and versatility: IRT cameras are lightweight and can be easily carried. This allows to choose different fixed installations leading to different field of views and spatial resolution of the investigated scenario.
5. Easy and fast data collection and processing: the recorded data can be easily collected, monitored and processed on laptops using dedicated imaging software, therefore allowing the measurements' repeatability.

6. Fast response rate: thermal imaging equipment used with a multi-temporal approach can detect and monitor rapid thermal fluctuations.
7. Orientation of the slope with respect to solar illumination: the slope aspect has an influence on the intensity and the time of exposure of the solar illumination which affects the slope. Surface temperature differences will be greater in sun-exposed surfaces.
8. Orientation and distance of the slope with respect to the operator: IRT camera field of view and the thermograms' spatial resolution strongly depend on the distance between the target and the object. Logistical problematics may impede a picture of the whole investigated scenario. The slope surface orientation with respect to the viewer also influences the amount of emitted and reflected thermal radiation measured by the sensor (the more the line of sight is perpendicular to the surface the higher the measured thermal radiation).
9. Dependence on weather conditions: high surface temperature differences are more easily detectable during warm spring and summer seasons. IRT camera measurements are negatively affected by strong wind (due to air convection) and rain (due to evaporation and subsequent cooling). The multi-temporal approach is not always suitable when it is necessary to acquire data as fast as possible.
10. Bureaucratic restrictions: airborne thermal measurements are also affected by bureaucratic issues because flights are not allowed over prohibited, restricted or temporarily forbidden areas for safety reasons, particularly during emergencies.

6. Conclusions

Within this work, the potential of IRT as a novel operational tool for 2D and 3D landslide surveying, mapping and characterization was explored in several instability processes (rockslides, rockfalls, earth flows-slumps) and risk management contexts. In particular, IRT was applied, both from terrestrial and airborne platforms, in an integrated approach with TLS and GPS for the detection and characterization of criticalities on unstable slopes, in order to evaluate the possible related hazardous scenarios. Given the portability and cost-effectiveness of modern thermal cameras, as well as the fast acquisition and processing times of thermographic data, IRT can be profitably applied in the field of landslide analysis, for the remote rapid mapping of surface temperature patterns with high spatial resolution. The use of modern high resolution thermal cameras, employed both in terrestrial (hand-held, tripod-mounted) or airborne based modes, can lead to the detection of landslides' structural and morphologic potentially hazardous features (structural discontinuities and open fractures, scarps, seepage and moisture zones, landslide drainage network and ponds). In rock slide assessment, the potential of IRT for fracture mapping can lead to the evaluation of the unstable rock wedges volume, representing crucial information for planning the proper risk reduction-monitoring measures. On unstable rock walls, IRT can be profitably applied for integrating TLS in the rock mass characterization, with special regard to seepage along key discontinuities and mapping potential unstable ledge-niche systems. Furthermore, accurate mapping of open fractures could provide useful information for the planning of a crack meter network for monitoring deformations. Mapping the drainage network and moisture areas in large earth roto-translational slide/flows can be useful for rapid mapping and for the temporal planning of adequate landslide restoration works. Nevertheless, IRT alone is insufficient for a complete landslide analysis. In order to obtain a more accurate interpretation of the results, IRT can be more profitably used as an ancillary low-cost technique, through integration with other ground-based remote sensing geodetic techniques, especially regarding TLS and DP. Future developments should include the application of fixed thermal camera installations in a landslide remote surveying-monitoring station, including e.g., GB-InSAR systems, for gathering continuous, high-resolution, real-time data. Furthermore, thanks to the high image resolution of the more recent thermal cameras (nowadays up to 1280 $\times$ 1024 pixel), thermographic data could be used in a photogrammetric approach in order to obtain terrain 3D surface temperature maps by directly using the thermograms, thus avoiding complex image geocoding

procedures on the TLS 3D surface. In this perspective, specific geometric calibration files could allow thermal cameras to be placed on top of TLS devices to produce a point cloud with thermal textures. Finally, the rapid evolution of IRT technology opens future scenarios of rapid automated inspections on hazardous scenarios, which could be further quickened by using remotely controlled drone platforms. In all of these perspectives, a skilled thermal camera operator is strongly recommended for correct IRT image acquisition, elaboration and interpretation procedures.

Acknowledgments: The authors would like to thank Massimiliano Nocentini for his constant encouragements, and Francesco Mugnai for the accurate revisions of the manuscript.

Author Contributions: W.F. conceived the article structure, collected, processed and analyzed the IRT data; G.G. and L.L. performed the TLS surveys, processed and analysed the related data, and performed the IRT-TLS data fusion; S.M. contributed to the field inspections and thermograms mosaicking; N.C. coordinated the project work, the paper's writing with special regards to the reviewing process.

Conflicts of Interest: The authors declare no conflict of interest.

References

1. Guzzetti, F. Landslide hazard assessment and risk evaluation: Limits and prospectives. In Proceedings of the 4th EGS Plinius Conference, Mallorca, Spain, 2–4 October 2002.
2. Guzzetti, F.; Mondini, A.C.; Cardinali, M.; Fiorucci, M.; Santangelo, M.; Chang, K.T. Landslide inventory maps: New tools for an old problem. *Earth Sci. Rev.* **2012**, *112*, 1–25. [CrossRef]
3. Casagli, N.; Frodella, W.; Morelli, S.; Tofani, V.; Ciampalini, A.; Intrieri, E.; Raspini, F.; Rossi, G.; Tanteri, L.; Lu, P. Spaceborne, UAV and ground-based remote sensing techniques for landslide mapping, monitoring and early warning. *Geoenviron. Disasters* **2017**, *4*, 9. [CrossRef]
4. Chandler, J. Effective application of automated digital photogrammetry for geomorphological research. *Earth Surf. Process. Landf.* **1999**, *24*, 51–63. [CrossRef]
5. Zhang, Z.; Zheng, S.; Zhan, Z. *Digital Terrestrial Photogrammetry with Photo Total Station*; International Archives of Photogrammetry and Remote Sensing: Istanbul, Turkey, 2004; pp. 232–236.
6. Sturzenegger, M.; Stead, D. Quantifying discontinuity orientation and persistence on high mountain rock slopes and large landslides using terrestrial remote sensing techniques. *Nat. Hazards Earth Syst. Sci.* **2009**, *9*, 267–287. [CrossRef]
7. Jaboyedoff, M.; Oppikofer, T.; Abellán, A.; Derron, M.H.; Loye, A.; Metzger, R.; Pedrazzini, A. Use of LIDAR in landslide investigations: A review. *Nat. Hazards* **2012**, *61*, 5–28. [CrossRef]
8. Frohlich, C.; Mettenleiter, M. Terrestrial laser scanning: New perspectives in 3D surveying. In *Laser Scanners for Forest and Landscape Assessment*; Part 8, W2; Thies, M., Koch, B., Spiecker, H., Weinacker, H., Eds.; International Archives of Photogrammetry, Remote Sensing and Spatial Information Sciences: Freiburg, Germany, 2004; Volume 36.
9. Abellán, A.; Oppikofer, T.; Jaboyedoff, M.; Rosser, N.J.; Lim, M.; Lato, M.J. Terrestrial laser scanning of rock slope instabilities. *Earth Surf. Process. Landf.* **2014**, *39*, 80–97. [CrossRef]
10. Tarchi, D.; Casagli, N.; Fanti, R.; Leva, D.; Luzi, G.; Pasuto, A.; Pieraccini, M.; Silvano, S. Landslide monitoring by using ground-based SAR interferometry: An example of application to the Tessina landslide in Italy. *Eng. Geol.* **2003**, *1*, 15–30. [CrossRef]
11. Fidolini, F.; Pazzi, V.; Frodella, W.; Morelli, S.; Fanti, R. Geomorphological characterization, monitoring and modeling of the Monte Rotolon complex landslide (Recoaro Terme, Italy). *Eng. Geol. Soc. Territ.* **2015**, *2*, 1311–1315.
12. Frodella, W.; Ciampalini, A.; Bardi, F.; Salvatici, T.; Di Traglia, F.; Basile, G.; Casagli, N. A method for assessing and managing landslide residual hazard in urban areas. *Landslides* **2017**, 1–15. [CrossRef]
13. Teza, G.; Marcato, G.; Castelli, E.; Galgaro, A. IRTROCK: A matlab toolbox for contactless recognition of surface and shallow weakness traces of a rock mass by infrared thermography. *Comput. Geosci.* **2012**, *45*, 109–118. [CrossRef]
14. Wu, J.H.; Lin, H.M.; Lee, D.H.; Fang, S.C. Integrity assessment of rock mass behind the shotcreted slope using thermography. *Eng. Geol.* **2005**, *80*, 164–173. [CrossRef]

15. Gigli, G.; Frodella, W.; Garfagnoli, F.; Morelli, S.; Mugnai, F.; Menna, F.; Casagli, N. 3-D geomechanical rock mass characterization for the evaluation of rockslide susceptibility scenarios. *Landslides* **2014**, *11*, 131–140. [CrossRef]
16. Spampinato, L.; Calvari, S.; Oppenheimer, C.; Boschi, E. Volcano surveillance using infrared cameras. *Earth Sci. Rev.* **2011**, *106*, 63–91. [CrossRef]
17. Maldague, X. *Theory and Practice of Infrared Technology for Non-Destructive Testing*; John-Wiley & Sons: Hoboken, NJ, USA, 2001; 684p.
18. Shannon, H.R.; Sigda, J.M.; Van Dam, R.L.; Hendrickx, J.M.; McLemore, V.T. Thermal camera imaging of rock piles at the Questa Molybdenum Mine, Questa, New Mexico. In Proceedings of the 22nd America Society of Mining and Reclamation Annual National Conference, Breckenridge, CO, USA, 19–23 June 2005; pp. 1015–1028.
19. Barla, G.; Antolini, F.; Gigli, G. 3D Laser scanner and thermography for tunnel discontinuity mapping. *Geomech. Tunn.* **2016**, *9*, 29–36. [CrossRef]
20. Campbell, C.W.; El Latif, A.; Foster, J.W. Application of thermography to karst hydrology. *J. Cave Karst Stud.* **1996**, *58*, 163–167.
21. Neale, C.M.U.; Sivarajan, S.; Akasheh, O.Z.; Jaworowski, C.; Heasler, H. Monitoring geothermal activity in Yellowstone National Park using airborne thermal infrared remote sensing. In Proceedings of the SPIE 7472, Remote Sensing for Agriculture, Ecosystems, and Hydrology XI, Berlin, Germany, 31 August–3 September 2009.
22. Neale, C.M.; Sivarajan, S.; Masih, A.; Jaworowski, C.; Heasler, H. Thermal remote sensing of snow cover to identify the extent of hydrothermal areas in Yellowstone National Park. In Proceedings of the SPIE 8531, Remote Sensing for Agriculture, Ecosystems, and Hydrology XIV, Edinburgh, UK, 24–27 September 2012; Volume 8531, pp. 853110–853116.
23. Hardgrove, C.; Moersch, J.; Whisner, S. Thermal imaging of alluvial fans: A new technique for remote classification of sedimentary features. *Earth Planet. Sci. Lett.* **2009**, *285*, 124–130. [CrossRef]
24. Hardgrove, C.; Moersch, J.; Whisner, S. Thermal imaging of sedimentary features on alluvial fans. *Planet. Space Sci.* **2010**, *58*, 482–508. [CrossRef]
25. Price, J. The potential of remotely sensed thermal infrared data to infer surface soil moisture and evaporation. *Water Resour. Res.* **1980**, *16*, 787–795. [CrossRef]
26. Coppola, A.; Basile, A.; Menenti, M.; Buonanno, M.; Colin, J.; De Mascellis, R.; Esposito, M.; Lazzaro, U.; Magliulo, V.; Manna, P. Spatial distribution and structure of remotely sensed surface water content estimated by a thermal inertia approach. In *Remote Sensing for Environmental Monitoring and Change Detection. Proceedings of Symposium HS3007 at IUGG, Perugia, Italy, July 2007*; International Association of Hydrological Sciences (IAHS)—IAHS Publ.: Oxfordshire, UK, 2007; Volume 316, pp. 1–12.
27. Eccel, E.; Arman, G.; Zottele, F.; Gioli, B. Thermal infrared remote sensing for high resolution minimum temperature mapping. *Ital. J. Agrometeorol.* **2008**, *13*, 52–61.
28. Moran, M.S.; Peters-Lidard, C.D.; Watts, J.M.; McElroy, S. Estimating soil moisture at the watershed scale with satellite-based radar and land surface models. *Can. J. Remote Sens.* **2004**, *30*, 805–826. [CrossRef]
29. Wilson, J.; Tian, G.; Mukriz, I.; Almond, D. PEC thermography for imaging multiple cracks from rolling contact fatigue. *NDT E Int.* **2011**, *44*, 505–512. [CrossRef]
30. Meola, C.; Carlomagno, G.M.; Squillace, A.; Giorleo, G. Non-destructive control of industrial materials by means of lock-in thermography. *Meas. Sci. Technol.* **2002**, *13*, 1583. [CrossRef]
31. Clark, M.R.; McCann, D.M.; Forde, M.C. Application of infrared thermography to the non-destructive testing of concrete and masonry bridges. *NDT E Int.* **2003**, *36*, 265–275. [CrossRef]
32. Tavukçuoğlu, A.; Düzgüneş, A.; Caner-Saltik, E.N.; Demirci, Ş. Use of IR thermography for the assessment of surface-water drainage problems in a historical building, Agzikarahan (Aksaray), Turkey. *NDT E Int.* **2005**, *38*, 402–410. [CrossRef]
33. Meola, C. Infrared thermography of masonry structures. *Infrared Phys. Technol.* **2006**, *49*, 228–233. [CrossRef]
34. Cabrelles, M.; Galcerá, S.; Navarro, S.; Lerma, J.L.; Akasheh, T.; Haddad, N. Integration of 3D laser scanning, photogrammetry and thermography to record architectoral monuments. In Proceedings of the 22nd CIPA Symposium, Kyoto, Japan, 11–15 October 2009.
35. Aggelis, D.G.; Kordatos, E.Z.; Soulioti, D.V.; Matikas, T.E. Combined use of thermography and ultrasound for the characterization of subsurface cracks in concrete. *Constr. Build. Mater.* **2010**, *24*, 1888–1897. [CrossRef]

36. Nolesini, T.; Frodella, W.; Bianchini, S.; Casagli, N. Detecting Slope and Urban Potential Unstable Areas by Means of Multi-Platform Remote Sensing Techniques: The Volterra (Italy) Case Study. *Remote Sens.* **2016**, *8*, 746. [CrossRef]
37. Fuad Khan, F.; Bolhassani, M.; Kontsos, A.; Hamid, A.; Bartoli, I. Modeling and experimental implementation of infrared thermography on concrete masonry structures. *Infrared Phys. Technol.* **2015**, *69*, 228–237. [CrossRef]
38. Bison, P.; Grinzato, E.; Pasuto, A.; Silvano, S. Thermal IR remote sensing in landslides survey. In Proceedings of the 6th International IAEG Congress, Rotterdam, The Netherlands, 6–10 August 1990; pp. 873–878.
39. Fiorillo, F.; Tulipano, L. Alcune applicazioni dell'infrarosso termico a tematiche geoapplicative. *Geol. Romana* **1992**, *30*, 395–402.
40. Squarzoni, C.; Galgaro, A.; Teza, G.; Acosta, C.A.T.; Pernito, M.A.; Bucceri, N. Terrestrial laser scanner and infrared thermography in rock fall prone slope analysis. *Geophys. Res. Abstr.* **2008**, *10*. EGU2008-A-09254, EGU General Assembly 2008.
41. Martino, S.; Mazzanti, P. Integrating geomechanical surveys and remote sensing for sea cliff slope stability analysis: The Mt. Pucci case study (Italy). *Nat. Hazards Earth Syst. Sci.* **2014**, *14*, 831. [CrossRef]
42. Baroň, I.; Bečkovský, D.; Míča, L. Application of infrared thermography for mapping open fractures in deep-seated rockslides and unstable cliffs. *Landslides* **2014**, *11*, 15–27. [CrossRef]
43. Teza, G.; Marcato, G.; Pasuto, A.; Galgaro, A. Integration of laser scanning and thermal imaging in monitoring optimization and assessment of rockfall hazard: A case history in the Carnic Alps (Northeastern Italy). *Nat. Hazards* **2015**, *76*, 1535–1549. [CrossRef]
44. Gigli, G.; Intrieri, E.; Lombardi, L.; Nocentini, M.; Frodella, W.; Balducci, M.; Venanti, L.D.; Casagli, N. Event scenario analysis for the design of rockslide countermeasures. *J. Mt. Sci.* **2014**, *11*. [CrossRef]
45. Adorno, V.; Barnobi, L.; La Rosa, F.; Leotta, A.; Paratore, M. Contributo della tecnologia laser scanner e termografia IR nella caratterizzazione geomeccanica di un costone roccioso. In Proceedings of the 13th ASITA National Conference, Bari, Italy, 1–4 December 2009.
46. Frodella, W.; Morelli, S.; Fidolini, F.; Pazzi, V.; Fanti, R. Geomorphology of the Rotolon landslide (Veneto Region, Italy). *J. Maps* **2014**, *10*, 394–401. [CrossRef]
47. Frodella, W.; Fidolini, F.; Morelli, S.; Pazzi, V. Application of Infrared Thermography for landslide mapping: The Rotolon DSGDS case study. *Rend. Online Soc. Geol. Ital.* **2015**, *35*, 144–147. [CrossRef]
48. Frodella, W.; Morelli, S.; Pazzi, V. Infrared Thermographic surveys for landslide mapping and characterization: The Rotolon DSGSD (Norther Italy) case study. *Ital. J. Eng. Geol. Environ.* **2017**. [CrossRef]
49. Mineo, S.; Pappalardo, G.; Rapisarda, F.; Cubito, A.; Di Maria, G. Integrated geostructural, seismic and infrared thermography surveys for the study of an unstable rock slope in the Peloritani Chain (NE Sicily). *Eng. Geol.* **2015**, *195*, 225–235. [CrossRef]
50. Pappalardo, G.; Mineo, S.; Zampelli, S.P.; Cubito, A.; Calcaterra, D. InfraRed Thermography proposed for the estimation of the Cooling Rate Index in the remote survey of rock masses. *Int. J. Rock Mech. Min. Sci.* **2016**, *83*, 182–196. [CrossRef]
51. Whitworth, M.C.Z.; Giles, D.P.; Murphy, W. Airborne remote sensing for landslide hazard assessment: A case study on the Jurassic escarpment slopes of Worcestershire, UK. *Q. J. Eng. Geol. Hydrogeol.* **2005**, *38*, 285–300. [CrossRef]
52. Stumpf, A.; Kerle, N.; Malet, J.P. Passive optical sensors. In *Review of Techniques for Landslide Detection, Fast Characterization, Rapid Mapping and Long-Term Monitoring*; Michoud, C., Abellán, A., Derron, M.-H., Jaboyedoff, M., Eds.; Deliverable 4.1 of the European Project SAFELAND: Sognsveien, Norway, 2010; Available online: http://www.safeland-fp7.eu (accessed on 24 June 2017).
53. Lillesand, T.M.; Kiefer, R.W.; Chipman, J.W. *Remote Sensing and Image Interpretation*, 6th ed.; John Wiley and Sons, Inc.: Hoboken, NJ, USA, 2008.
54. Bhowmik, M.K.; Saha, K.; Majumder, S.; Majumder, G.; Saha, A.; Sarma, A.N.; Bhattacharjee, D.; Basu, D.K.; Nasipuri, M. Thermal infrared face recognition a biometric identification technique for robust security system. In *Reviews, Refinements and New Ideas in Face Recognition*; InTech: Rijeka, Croatia, 2011; pp. 113–138.
55. Dhar, N.K.; Sood, A.K.; Dat, R. *Advances in Infrared Detector Array Technology*; InTech: Rijeka, Croatia, 2013.
56. Incropera, P.F.; De Witt, D.P. *Introduction to Heat Transfer*; John Wiley: Hoboken, NJ, USA, 1985; pp. 654–746.
57. Rees, W.G. *Physical Principles of Remote Sensing*, 2nd ed.; Cambridge University Press: Cambridge, UK, 2001.
58. Jones, H.G. Use of thermography for quantitative studies of spatial and temporal variation of stomatal conductance over leaf surfaces. *Plant Cell Environ.* **1999**, *22*, 1043–1055. [CrossRef]

59. Ballestracci, R.; Nougier, J. Detection by infrared thermography and modelling of an ice capped geothermal system in Kerguelen archipelago. *J. Volcanol. Geotherm. Res.* **1984**, *20*, 85–99. [CrossRef]
60. Rogalski, A. Recent progress in infrared detector technologies. *Infrared Phys. Technol.* **2011**, *54*, 136–154. [CrossRef]
61. FLIR Systems Inc., ThermaCAM SC620 Technical Specifications. 2009. Available online: http://www.flir.com/cs/emea/en/view/?id=41965 (accessed on 5 June 2017).
62. FLIR Systems Inc., Reporter Professional 9. 2012. Available online: http://www.flir.com/cs/emea/en/view/?id=42405 (accessed on 5 June 2017).
63. FLIR Systems Inc., ResearchIR 3.4. sp3. 2013. Available online: http://support.flir.com/DsDownload/Assets/T198206_en_40.pdf (accessed on 5 June 2017).
64. Cruden, D.M.; Varnes, D.J. Landslide types and processes. In *Landslides: Investigation and Mitigation: Sp. Rep. 247, Transportation Research Board, National Research Council*; Turner, A.K., Schuster, R.L., Eds.; National Academy Press: Washington, DC, USA, 1996; pp. 36–75.
65. FLIR Systems Inc. *ThermaCAM SC620 User's Manual*; FLIR Systems Inc.: Wilsonville, OR, USA, 2009.
66. Avdelidis, N.P.; Moropoulou, A. Emissivity considerations in building thermography. *Elsevier Sci. Energy Build.* **2003**, *35*, 663–667. [CrossRef]
67. Kotthaus, S.; Smith, T.E.; Wooster, M.J.; Grimmond, C.S.B. Derivation of an urban materials spectral library through emittance and reflectance spectroscopy. *ISPRS J. Photogramm. Remote Sens.* **2014**, *94*, 194–212. [CrossRef]
68. Salisbury, J.W.; D'Aria, D.M. Emissivity of terrestrial materials in the 8–14 μm atmospheric window. *Remote Sens. Environ.* **1992**, *42*, 83–106. [CrossRef]
69. Riscan Pro 2.0. Data Sheet of Riscan Pro 2.0. Available online: http://www.riegl.com/uploads/tx_pxpriegldownloads/11_DataSheet_RiSCAN-PRO_2016-09-19_01.pdf (accessed on 5 June 2017).
70. Intrieri, E.; Gigli, G.; Mugnai, F.; Fanti, R.; Casagli, N. Design and implementation of a landslide early warning system. *Eng. Geol.* **2012**, *147*, 124–136. [CrossRef]
71. Graziani, A.; Rotonda, T.; Tommasi, P. Stability and deformation mode of a rock slide along interbeds reactivated by rainfall. In Proceedings of the 1st Italian Workshop on Landslides, Napoli, Naples, Italy, 8–10 June 2009; Volume 1, pp. 62–71.
72. Frodella, W.; Ciampalini, A.; Gigli, G.; Lombardi, L.; Raspini, F.; Nocentini, M.; Scardigli, C.; Casagli, N. Synergic use of satellite and ground based remote sensing methods for monitoring the San Leo rock cliff (Northern Italy). *Geomorphology* **2016**, *264*, 80–94. [CrossRef]
73. Nesci, O.; Savelli, D.; Diligenti, A.; Marinangeli, D. Geomorphological sites in the northern marche (Italy). Examples from autochton anticline ridges and from Val Marecchia allochton. *Ital. J. Quat. Sci.* **2005**, *18*, 79–91.
74. Ribacchi, R.; Tommasi, P. Preservation and protection of the historical town of San Leo (Italy). In Proceedings of the IAEG International Symposium on Engineering Geology of Ancient Works, Monuments and Hitorical Sites, Athens, Greece, 19–23 September 1988; Volume 1, pp. 55–64.
75. ISRM (International Society for Rock Mechanics and Rock Engineering). Commission on the standardization of laboratory and field test. Suggested methods for the quantitative description of discontinuities in rock masses. *Int. J. Rock Mech. Min. Sci. Geomech. Abs.* **1978**, *15*, 319–368.
76. Bardi, F.; Raspini, F.; Frodella, W.; Lombardi, L.; Nocentini, M.; Gigli, G.; Morelli, S.; Corsini, A.; Casagli, N. Monitoring the Rapid-Moving Reactivation of Earth Flows by Means of GB-InSAR: The April 2013 Capriglio Landslide (Northern Appennines, Italy). *Remote Sens.* **2017**, *9*, 165. [CrossRef]
77. Bardi, F.; Raspini, F.; Frodella, W.; Lombardi, L.; Nocentini, M.; Gigli, G.; Morelli, S.; Corsini, A.; Casagli, N. Remote Sensing Mapping and Monitoring of the Capriglio Landslide (Parma Province, Northern Italy). *Adv. Cult. Living Landslides* **2017**, *3*, 231–238, Advances in Landslide Technology.
78. Lombardi, L.; Nocentini, M.; Frodella, W.; Nolesini, T.; Bardi, F.; Intrieri, E.; Ferrigno, F.; Solari, L.; Carlà, T.; Casagli, N. The Calatabiano landslide (southern Italy): Preliminary GB-InSAR monitoring data and remote 3D mapping. *Landslides* **2016**, *14*, 685–696. [CrossRef]
79. Nolesini, T.; Frodella, W.; Lombardi, L.; Nocentini, M.; Bardi, F.; Intrieri, E.; Carlà, T.; Solari, L.; Dotta, G.; Ferrigno, F.; et al. Remote 3D Mapping and GB-InSAR Monitoring of the Calatabiano Landslide (Southern Italy). *Adv. Cult. Living Landslides* **2017**, *3*, 277–284, Advances in Landslide Technology.

80. Guzzetti, F.; Reichenbach, P.; Cardinali, M.; Galli, M.; Ardizzone, F. Probabilistic landslide hazard assessment at the basin scale. *Geomorphology* **2005**, *72*, 272–299. [CrossRef]
81. Parker, R.N.; Densmore, A.L.; Rosser, N.J.; de Michele, M.; Li, Y.; Huang, R.; Whadcoat, S.; Petley, D.N. Mass wasting triggered by the 2008 Wenchuan earthquake is greater than orogenic growth. *Nat. Geosci.* **2011**, *4*, 449–452. [CrossRef]
82. Brunsden, D. Landslide types, mechanisms, recognition, identification. In *Landslides in the South Wales Coalfield, Proceedings Symposium*; Morgan, C.S., Ed.; The Polytechnic of Wales: South Wales, UK, 1985; pp. 19–28.
83. Santangelo, M.; Cardinali, M.; Rossi, M.; Mondini, A.C.; Guzzetti, F. Remote landslide mapping using a laser rangefinder binocular and GPS. *Nat. Hazards Earth Syst. Sci.* **2010**, *10*, 2539–2546. [CrossRef]
84. Hungr, O.; Evans, S.G. The occurrence and classification of massive rock slope failure. *Felsbau* **2004**, *22*, 16–23.
85. Margielewski, W.; Urban, J. Crevice-type caves as initial forms of rock landslide development in the Flysch Carpathians. *Geomorphology* **2003**, *54*, 325–338. [CrossRef]
86. Hungr, O. *Mobility of Rock Avalanches*; Report of the International Research Institute for Earth Science and Disaster Prevention; National Research Institute for Earth Science and Disaster Prevention: Tsukuba, Japan, 1990; Volume 46, pp. 11–19.
87. Legros, F. The mobility of long-runout landslides. *Eng. Geol.* **2002**, *63*, 301–331. [CrossRef]
88. Baum, R.L.; Godt, J.W. Early warning of rainfall-induced shallow landslides and debris flows in the USA. *Landslides* **2010**, *7*, 259–272. [CrossRef]
89. Rubio, E.; Caselles, V.; Badenas, C. Emissivity measurements of several soils and vegetation types in the 8–14 μm wave band: Analysis of two field methods. *Remote Sens. Environ.* **1997**, *59*, 490–521. [CrossRef]
90. Buongiorno, M.F.; Realmuto, V.J.; Fawzi, D. Recovery of spectral emissivity from thermal infrared multispectral scanner imagery acquired over a mountainous terrain: A case study from Mount Etna Sicily. *Remote Sens. Environ.* **2002**, *79*, 123–133. [CrossRef]
91. Dash, P.; Göttsche, F.M.; Olesen, F.S.; Fisher, H. Land surface temperature and emissivity estimation from passive sensor data: Theory and practice-current trends. *Int. J. Remote Sens.* **2002**, *23*, 2563–2594. [CrossRef]
92. Merucci, L.; Bogliolo, M.P.; Buongiorno, M.F.; Teggi, S. Spectral emissivity and temperature maps of the Solfatara crater from DAIS hyperspectral images. *Ann. Geophys.* **2006**, *49*. [CrossRef]
93. Ball, M.; Pinkerton, H. Factors affecting the accuracy of thermal imaging cameras in volcanology. *J. Geophys. Res.* **2006**, *111*, B11203. [CrossRef]